Electronic Supplementary Information

Self-supported NiTe@NiMo electrodes enabling efficient sulfion oxidation reaction toward energy-saving and chlorine-free hybrid seawater electrolysis at high current densities

Hao Tan, [‡a, b] *Zhipeng Yu,* [‡a] *Chenyue Zhang,*[a] *Fei Lin,* *[a] *Shiyu Ma,*[b] *Haoliang Huang,*[a] *Hong Li,*[b] *Dehua Xiong**[b] *and Lifeng Liu**[a]

[a] Songshan Lake Materials Laboratory (SLAB), Dongguan 523808, P. R. China

E-mail: linfei@sslab.org.cn, liu.lifeng@sslab.org.cn

[b] State Key Laboratory of Silicate Materials for Architectures, Wuhan University of Technology, Wuhan 430070, P. R. China

E-mail: xiongdehua@whut.edu.cn

H. Tan and Z. P. Yu contributed equally.

Experimental section

Reagents

Sodium tellurite (Na_2TeO_3, 99.9%, Adamas-beta), sodium molybdate dihydrate ($Na_2MoO_4·2H_2O$, 99.0%, Macklin), sodium borohydride ($NaBH_4$, 98%, Xihua), potassium hydroxide (KOH, 90.0%, Macklin), hydrochloric acid (HCl, 36~38%, Xihua), ethanol (CH_3CH_2OH, 99.7%, Xihua), sodium chloride (NaCl, 99.5%, Macklin), isopropanol (C_3H_8O, 99.5%, Macklin), sodium sulfide nonahydrate ($Na_2S·9H_2O$, 98%, Macklin), Pt/C catalysts (20 wt.% Pt, Innochem), ruthenium(IV) oxide (RuO_2, 99.9%, Alfa Aesar) and nickel nitrate hexahydrate ($Ni(NO_3)_2·6H_2O$, 98.0%, Xihua) were used as received for materials synthesis and electrolyte preparation. Deionized (DI) water (resistivity: 18.2 MΩ cm) was employed to prepare precursor solutions and electrolytes. Nickle foam (110 ppi, thickness: 1.0 mm) was purchased from Kunshan Xingzhenghong Electronic Materials Co., Ltd, China.

Synthesis of self-supported electrodes

A piece of nickel foam (NF, 3.0 cm × 4.0 cm) was immersed in 1.0 mol L^{-1} HCl solution and then ultrasonicated for 10 min to remove the surface oxide layer. Subsequently, it was carefully cleaned in DI water and ethanol in sequence, each for 10 min, to remove remanent impurities. Afterward, the NF was dried in a vacuum oven at 60 °C for 12 h.

The self-supported NiTe/NF electrode was fabricated by a hydrothermal method reported previously.[S1] Specifically, 1.0 mM Na_2TeO_3 powder was dissolved in 65.0 mL of DI water and the solution was continuously stirred for 10 min at room temperature. Then 5.0 mM $NaBH_4$ was added into the solution, which was subjected to vigorous stirring for 30 min. Subsequently, the solution was transferred into a 100 mL polytetrafluoroethylene (PTFE) lined stainless-steel autoclave reactor. After immersing the cleaned NF in the solution, the reactor was heated to 140 °C in an oven and maintained at this temperature for 20 h. Finally, the reactor was cooled

naturally down to room temperature. The foam was then taken out, washed with anhydrous ethanol and DI water sequentially, and dried in a vacuum oven at 60 °C for 12 h.

To obtain the NiTe@NiMo/NF electrode, we performed electrodeposition in a three-electrode cell using NiTe/NF (1.0 cm × 3.0 cm) as the working electrode, and an encapsulated platinum (Pt) coil and a saturated calomel electrode (SCE) as the counter and reference electrodes, respectively. The electrodeposition was carried out in a mixed solution of $Ni(NO_3)_2 \cdot 6H_2O$ (0.15 mol L^{-1}) and $Na_2MoO_4 \cdot 2H_2O$ (0.15 mol L^{-1}), the pH value of which is 6.8. The volume of the solution was approximately 70 mL, and solution resistance between the working and reference electrodes was about 3.5 Ω. The deposition was conducted in the constant potential mode at −0.9 V vs. SCE for various durations (1, 3, 5, 8, and 10 min), and no solution resistance compensation was adopted. Afterward, the electrode was carefully cleaned several times with DI water, and then dried at 60 °C in vacuum for 12 h. To make comparison, the deposition was also performed on a bare NF in the same electrolyte for 5 min, and the as-obtained sample is denoted as NiMo/NF. Moreover, commercial Pt/C and RuO_2 catalysts were also drop-cast on NF for use as controls. Specifically, 15 mg of Pt/C were dispersed in 1.0 mL of mixed solution containing 20 μL Nafion® solution, 245 μL H_2O and 735 μL C_3H_8O to make an ink. Subsequently, 100 μL of ink (about 1.5 mg Pt/C) were cast onto a bare NF with an exposed area of 1.0 cm^2 using a micropipette, leading to a Pt loading mass of about 0.3 mg cm^{-2}. Similar procedures were employed to prepare the RuO_2 control (Ru loading mass: 0.76 mg cm^{-2}).

Materials characterization

The crystalline structures of the prepared catalysts were examined by XRD (PANalytical, 40 kV, 15 mA) with Cu K_α radiation (λ = 1.541874 Å) and a PIXcel detector. The morphology, microstructure, and chemical composition of the catalysts were determined by FE-SEM (Verios 5UC, Thermo Fisher Scientific) and TEM (Tecnai F20, FEI) equipped with energy-dispersive X-ray spectroscopy (EDS). For TEM examination, the catalysts were peeled off from the NF

surface using a PTFE knife, and then dispersed in DI water by ultrasonication. The suspension was subsequently drop-cast on a carbon-coated copper grid which was later on dried under the irradiation of an IR baking lamp. The surface composition and chemical states of the self-supported electrodes were investigated by XPS (Thermo Escalab 250Xi, Thermo Fisher Scientific). All XPS spectra were calibrated with respect to the binding energy of C 1s (284.8 eV). Raman spectra were collected on a Horiba LabRam HR Evolution Raman microscope with a 532 nm laser. The UV-visible spectra of the electrolyte were obtained using a spectrometer (UV-Vis, HATACHI UH4150) working in the absorption mode. The XAS spectra were acquired at the BL14W1 beamline of the Shanghai Synchrotron Radiation Facility (SSRF, China) and B18 beamline of Diamond Light Source in the United Kingdom using a Si (311) double crystal monochromator. The NiTe@NiMo and NiTe catalysts were scraped off from the NF substrate, and then collected and pressed into circular disks for the XAS characterization.

The volume of H_2 generated was measured using a gas chromatograph (GC SP-3530, Beijing Beifen-Ruili Analytical Instrument (Group) Co., Ltd.), and Ar was used as the carrier gas during the measurements. The Faradic efficiency (FE) of H_2 production was then calculated according to the following equation:

$$\mathrm{FE} = \frac{2FVvp_0}{RTI} \times 100\% \quad \text{(S1)}$$

where v (Vol%) is the volume concentration of H_2 in the cathodic compartment of the H-cell, V is the gas flow rate measured (40 mL min^{-1}), F represents the Faradaic constant (96485 C mol^{-1}), p_0 stands for a standard atmospheric pressure (1.01×10^5 N m^{-2}), R is the ideal gas constant (8.314 N·m mol^{-1} K^{-1}), T denotes the temperature (298.15 K), and I (A) is the steady state cell current.

Electrochemical measurements

The electrocatalytic OER performance of the self-supported NiTe@NiMo/NF electrode and other references was evaluated in a three-electrode cell using an electrochemical workstation

(Bio-logic SAS, VMP-3e). The SOR performance was tested in an H-cell separated by a proton exchange membrane (Nafion® NR212). A Pt coil and a SCE encapsulated in the Luggin tube with a salt bridge were used as the counter and reference electrodes, respectively, and the prepared self-supported electrode (the area immersed in the electrolyte is 1 cm^2) as the working electrode. All potentials are converted to the reversible hydrogen electrode (RHE) scale according to the following equation:

$$U_{\mathrm{RHE}} = U_{\mathrm{SCE}} + 0.0591 \times \mathrm{pH} + 0.241 \quad \text{(S2)}$$

The OER performance was appraised in a simulated seawater consisting of 1.0 M KOH + 0.5 M NaCl (pH = 13.7). For the SOR-assisted seawater electrolysis, different concentrations (0.1, 0.3, 0.5, 0.7, 1.0, and 1.3 M) of $Na_2S{\cdot}9H_2O$ were added into the simulated seawater, and the pH values of these solutions remained virtually the same. Meanwhile, we also evaluated the OER and SOR performance in natural seawater (information about the location and time of acquisition is given in **Figure S30a**), and the pH and conductivity values of relevant solutions are presented in the Supplementary Information (**Table S8**). Before the electrochemical tests in natural seawater, 1.0 M KOH was added into the natural seawater to remove Ca^{2+} and Mg^{2+} cations. Solid precipitates were immediately observed, which are mainly composed of $Ca(OH)_2$ and $Mg(OH)_2$ (**Figure S30b**). The remaining clear solution was then filtered and used in the subsequent electrochemical tests. Cyclic voltammetry (CV) for the OER performance was performed in the range of 1.05 – 1.75 V vs. RHE at a scan rate of 2 mV s^{-1}, and the reduction branch of the CV curves was used to compare the OER performance of all electrodes. The SOR performance was evaluated at the same scan rate in the potential range of 0.15 – 0.60 V vs. RHE. To compensate for the voltage-drop between the reference and working electrodes, 85% iR correction was applied, unless otherwise specified. In order to study the charge transfer at the electrode/electrolyte interfaces, the potentiostatic electrochemical impedance spectroscopy (PEIS) was conducted at 1.45 V vs. RHE for the OER and 0.4 V vs. RHE for the SOR, respectively. The frequency range was set to 0.01 Hz – 100 kHz, with a 10 mV sinusoidal

perturbation. The obtained Nyquist plots were then fitted with the Z-View software. To calculate the electrochemical double-layer capacitance (C_{dl}), CV curves were recorded in the non-Faradaic region (1.0 – 1.1 V vs. RHE) at different scan rates (20, 40, 60, 80, 100 and 120 mV s^{-1}). Afterward, the C_{dl} values were obtained by linear fitting of the plots of average current density $|j_a - j_c|/2$ (j_a and j_c are the oxidative and reducing current density at 1.05 V vs. RHE, respectively) against the scan rate. Furthermore, the electrochemically active surface area (ECSA) was computed upon dividing C_{dl} by the specific capacitance (C_s) of a smooth electrode surface. C_s is assumed to be 0.04 mF cm^{-2} according to previous literature reports.[S2]

Calculation of hydrogen production rate and energy consumption

The energy consumption is calculated according to the following formula:

$$E = \frac{1(\text{mol}) \times 2 \times 96500(\text{C mol}^{-1})}{3600 \times 22.43 \times 10^{-3}(\text{m}^3 \cdot \text{mol}^{-1}) \times 1(\text{mol})} = 2390 \text{ Ah m}^{-3} \quad \text{(S3)}$$

$$Q = \frac{I \cdot n \cdot \eta}{E} \quad \text{(S4)}$$

$$W_d = \frac{E \cdot U}{1000 \cdot n} \quad \text{(S5)}$$

E: Theoretical electricity of produce 1.0 m^3 H_2 under standard conditions (Ah m^{-3});

Q: The production rate of H_2, (m^3 h^{-1});

W_d: The direct current specific energy consumption values (kWh m^{-3});

I: The direct current through the electrolysis cell chamber (A);

n: Number of electrolytic chambers, n = 1 in this work;

η: Current efficiency, assumed to be 100%;

U: Direct-current voltage of the electrolytic cell (V).

DFT calculations

All DFT calculations were performed using the Vienna Ab Initio Simulation Package (VASP).[S3, S4] The generalized gradient approximation method with the Perdew-Burke-Ernzerhof (PBE) exchange-correlation function was used to compute the electron exchange and

correlation energy.[S5] The plane wave basis (kinetic energy cut-off value: 450 eV) was employed to describe the valence electrons. All calculations were made based on the k-point sampling obtained from the gamma center with a mesh of 9 × 6 × 2. The atomic positions were fully optimized until the energy and forces were converged to 1×10^{-5} eV and 0.03 eV $Å^{-1}$, respectively. ISPIN was set to 2 since Ni is present in the model catalysts. The adsorption energy of each step of the SOR was calculated according to the following formula:

$$E_{\mathrm{ads}} = E_{*\mathrm{x}} - \left(E_{\mathrm{sys}} + E_{\mathrm{x}}\right) \tag{S6}$$

where $E_{*\mathrm{x}}$, E_{sys} and E_{x} are the total energy of the system, the system without X and with X, respectively, and X denotes the intermediate generated during the SOR. The chemical bonding analysis based on the crystal orbital Hamilton population (COHP) was carried out using the LOBSTER code.[S6, S7]

Supplementary Figures:

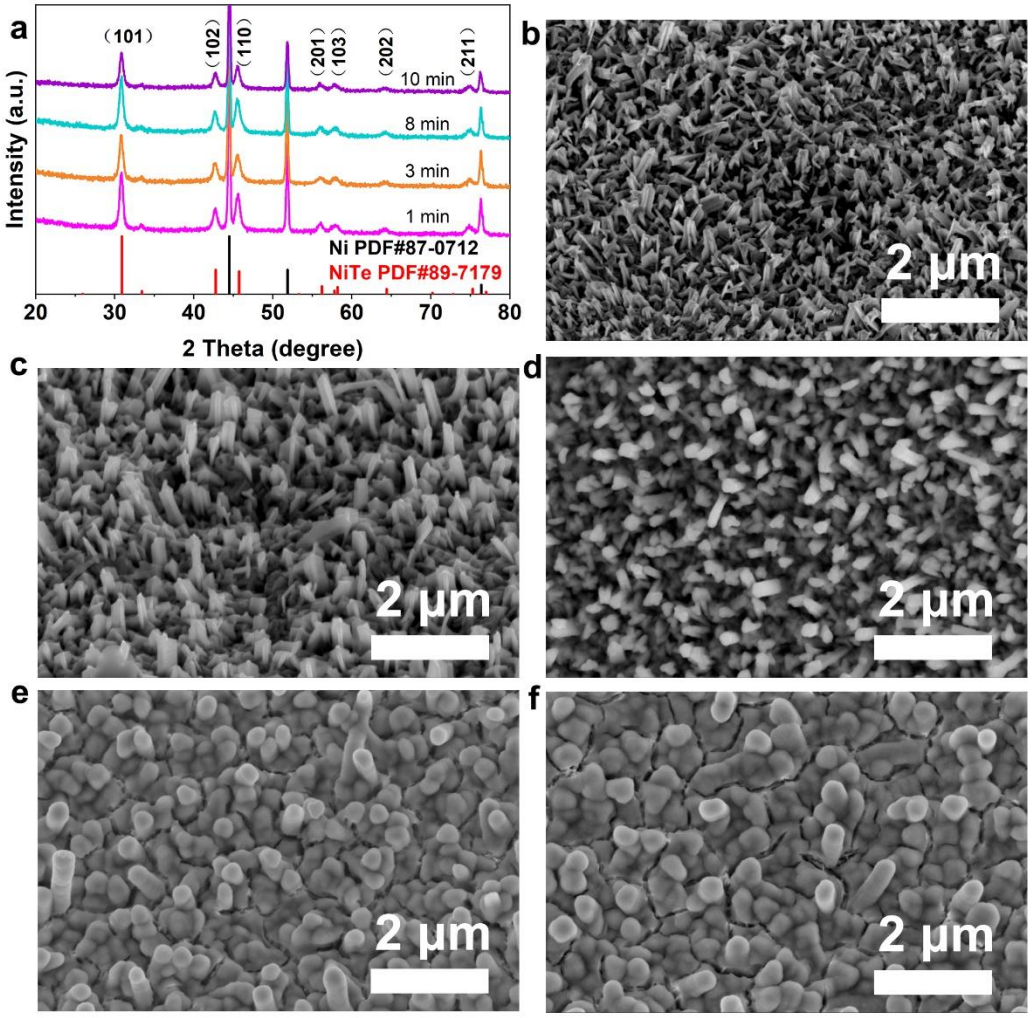

Fig. S1. (a) XRD patterns. SEM images of (b) NiTe/NF and NiTe@NiMo/NF after NiMo electrodeposition for (c) 1 min, (d) 3 min, (e) 8 min and (f) 10 min.

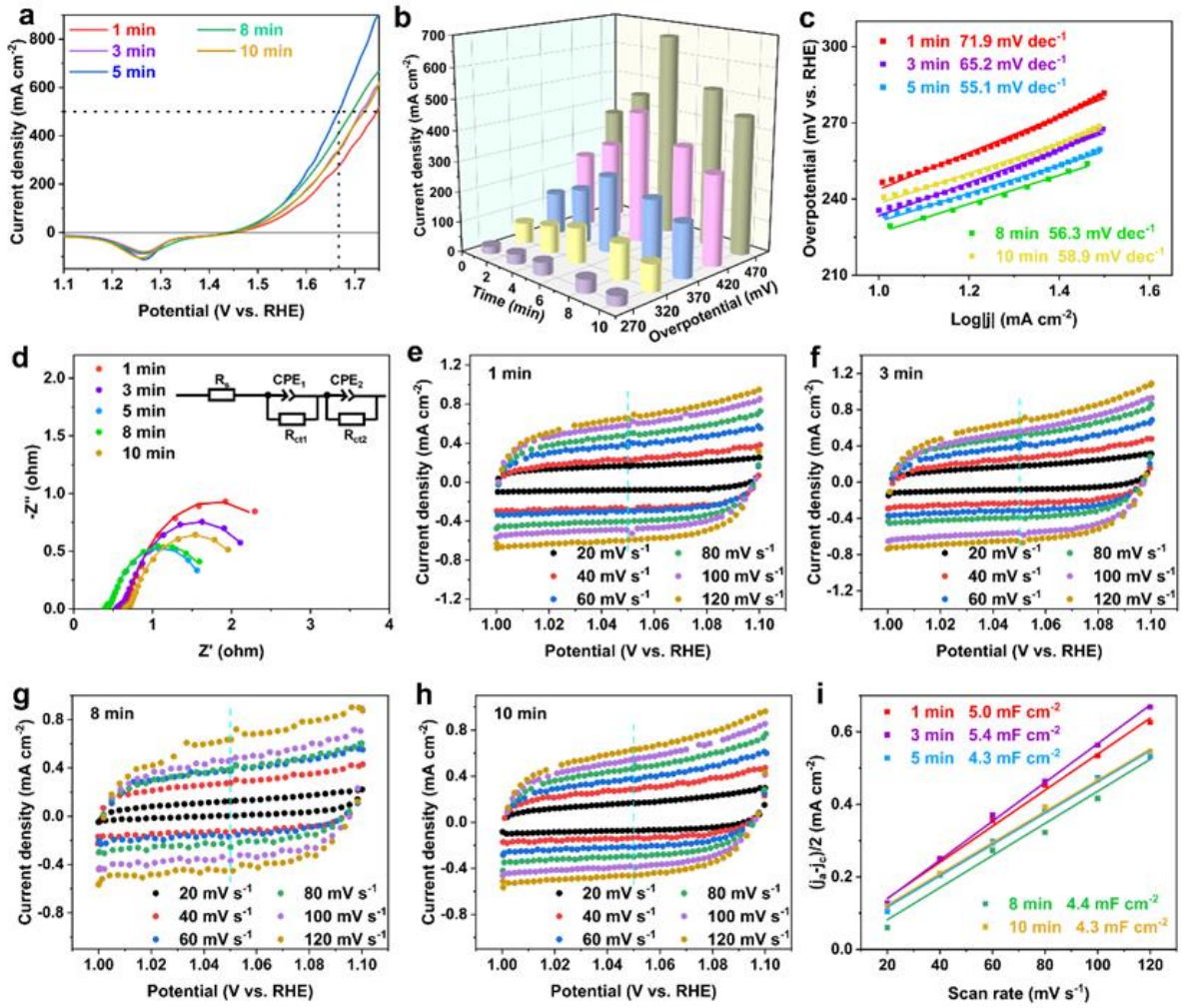

Fig. S2. The OER performance of NiTe@NiMo/NF electrodes with different NiMo loadings (NiMo electrodeposition for 1, 3, 5, 8 and 10 min) tested in simulated alkaline-saline water (Electrolyte: 1.0 M KOH + 0.5 M NaCl). (a) Polarization curves. (b) Comparison of the OER current densities generated by different electrodes at various overpotentials. (c) Tafel plots. (d) Nyquist plots. The solid lines are fitting curves. Inset: the equivalent circuit used for fitting. (e-h) CV plots at various scan rates for the NiTe@NiMo/NF electrodes with different NiMo loadings. (i) C_{dl} plots.

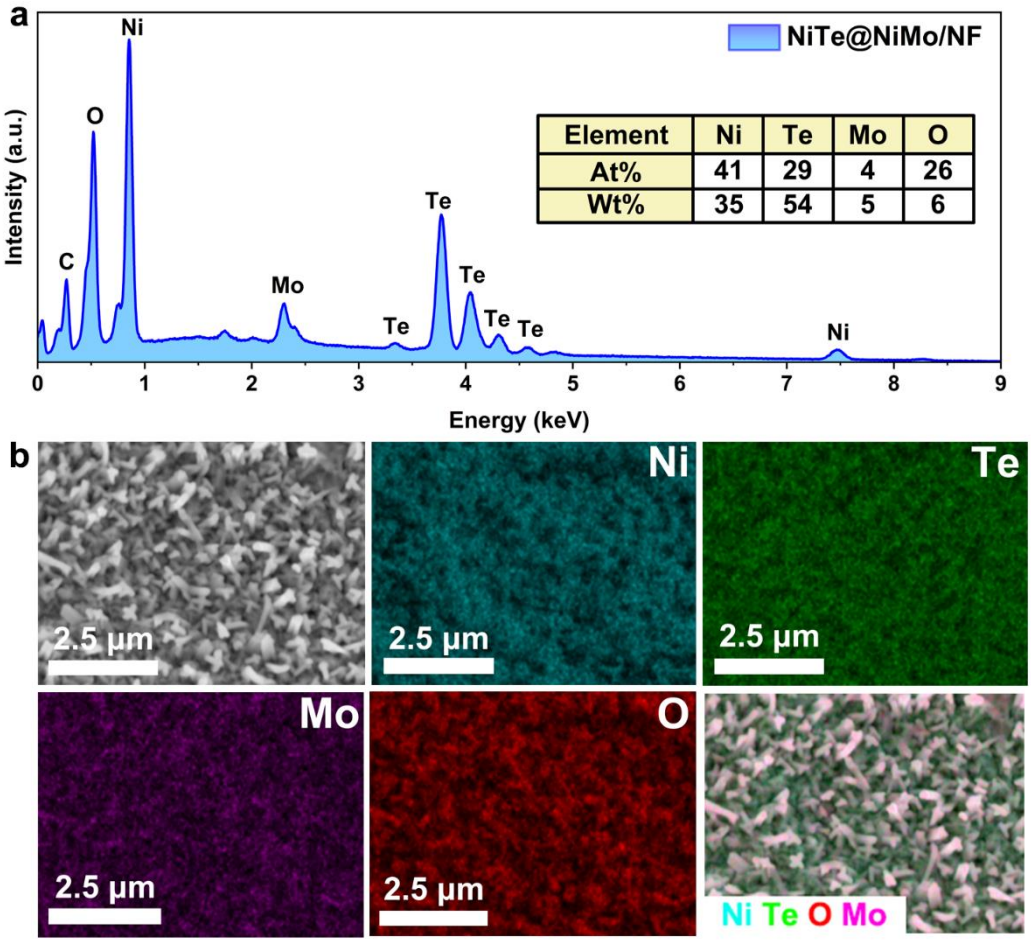

Fig. S3. (a) SEM-EDS spectrum, (b) SEM image and the corresponding elemental maps of the NiTe@NiMo/NF electrode. Inset of panel (a): elemental quantification by SEM-EDS.

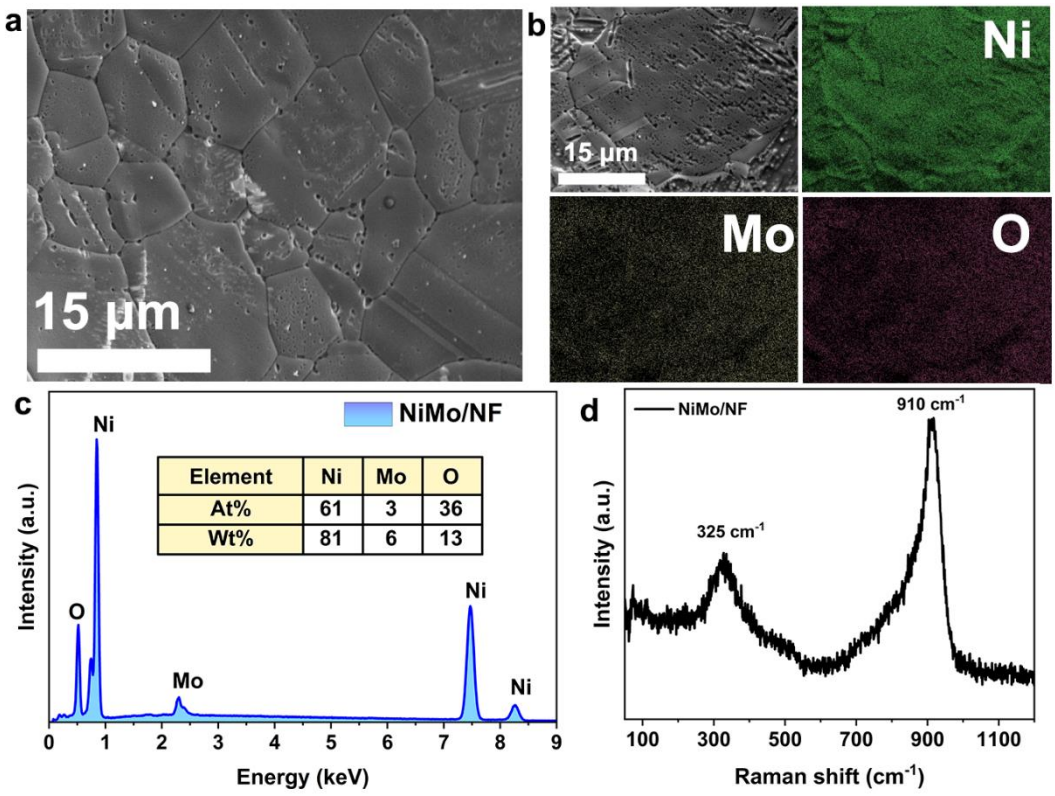

Fig. S4. (a) SEM image, (b) Elemental maps, (c) EDS spectrum and (d) Raman spectrum of the NiMo/NF reference electrode. Inset of panel (c): elemental quantification by SEM-EDS.

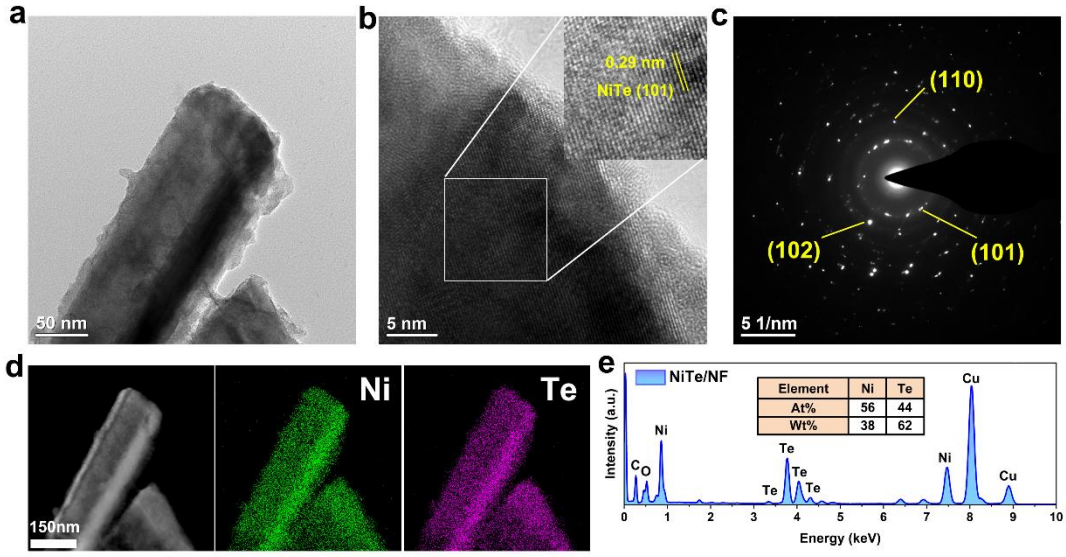

Fig. S5. (a) TEM image. (b) HRTEM image. Inset: zoomed view of a selected area marked by the white square. (c) SAED pattern. (d) elemental maps and (e) TEM-EDS spectrum of NiTe nanorods. Inset of panel (e): elemental quantification by TEM-EDS.

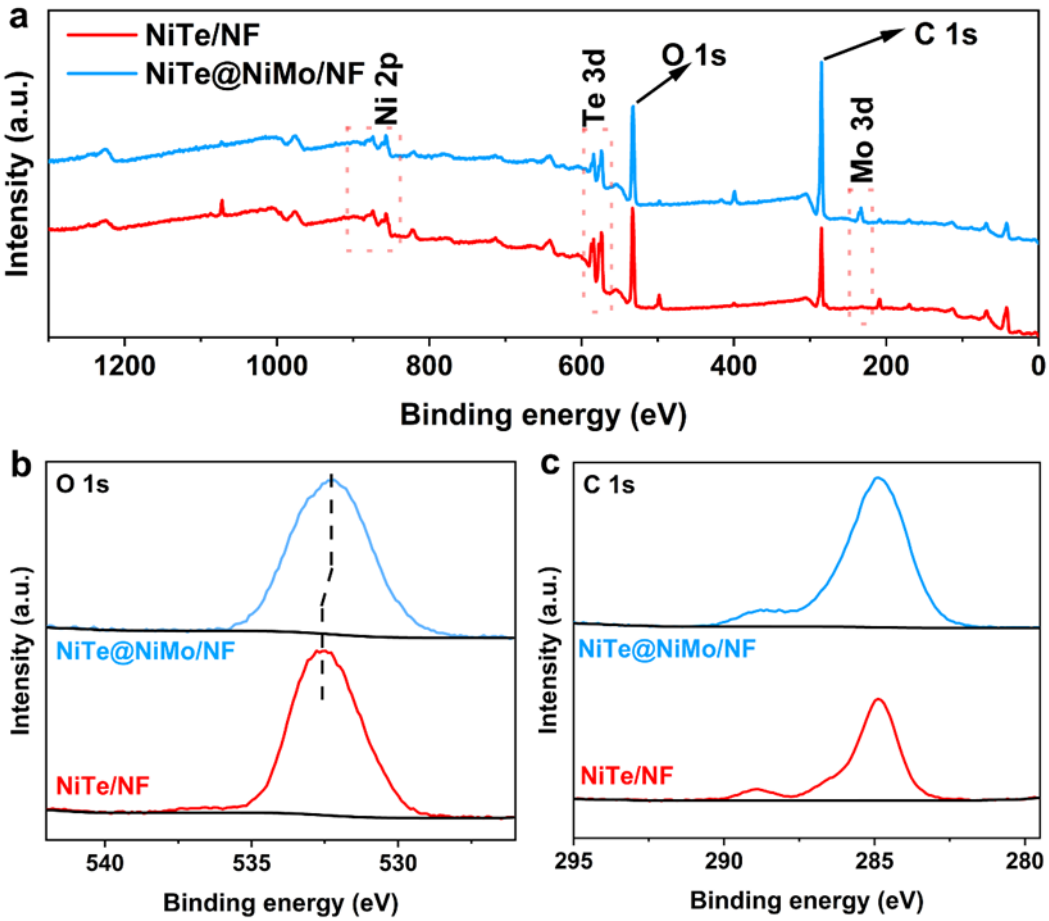

Fig. S6. (a) XPS survey spectra. High-resolution (b) O 1s and (c) C 1s spectra of the NiTe@NiMo/NF and NiTe/NF electrodes.

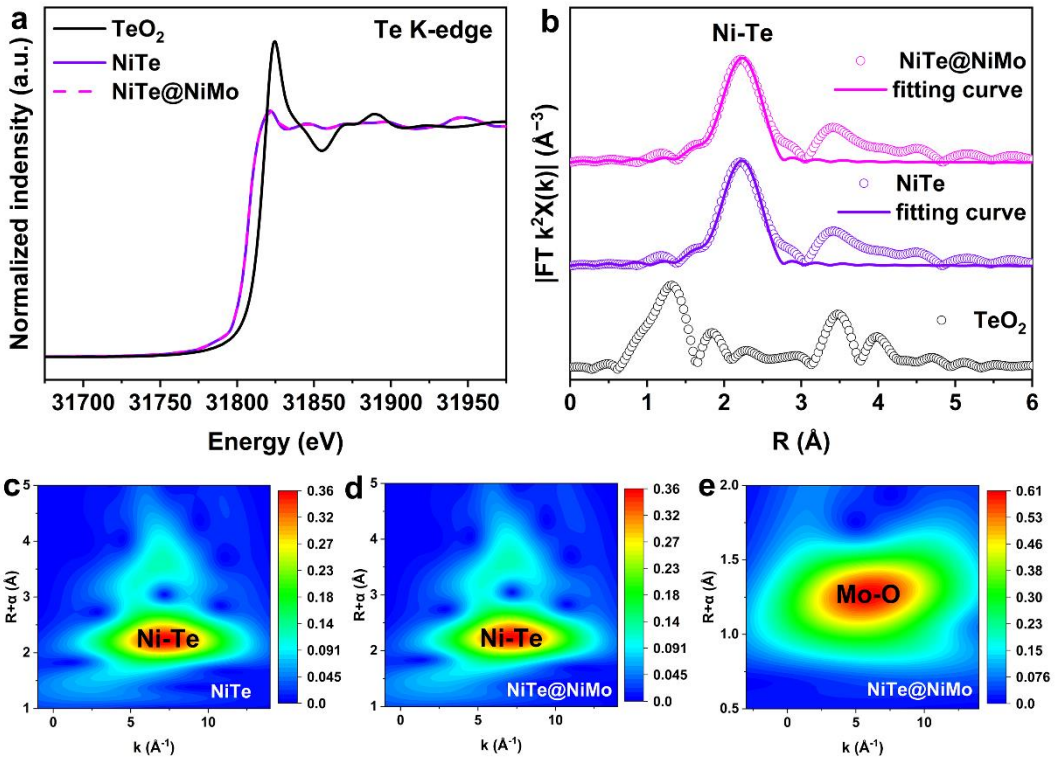

Fig. S7. XAS characterization of NiTe and NiTe@NiMo catalysts. (a) Te K-edge XANES spectra. (b) Fourier transforms of the k^2-weighted Te K-edge EXAFS spectra. Wavelet transform contours of (c) NiTe and (d-e) NiTe@NiMo.

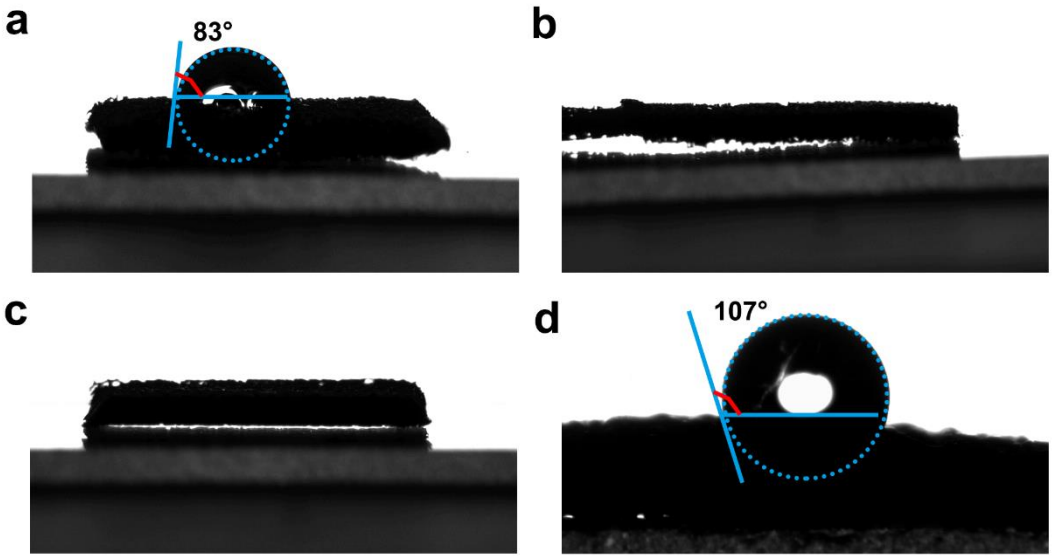

Fig. S8. Photographs showing the contact angle between simulated seawater (1.0 M KOH + 0.5 M NaCl) and (a) bare Ni foam, (b) NiTe/NF, (c) NiTe@NiMo/NF and (d) NiMo/NF.

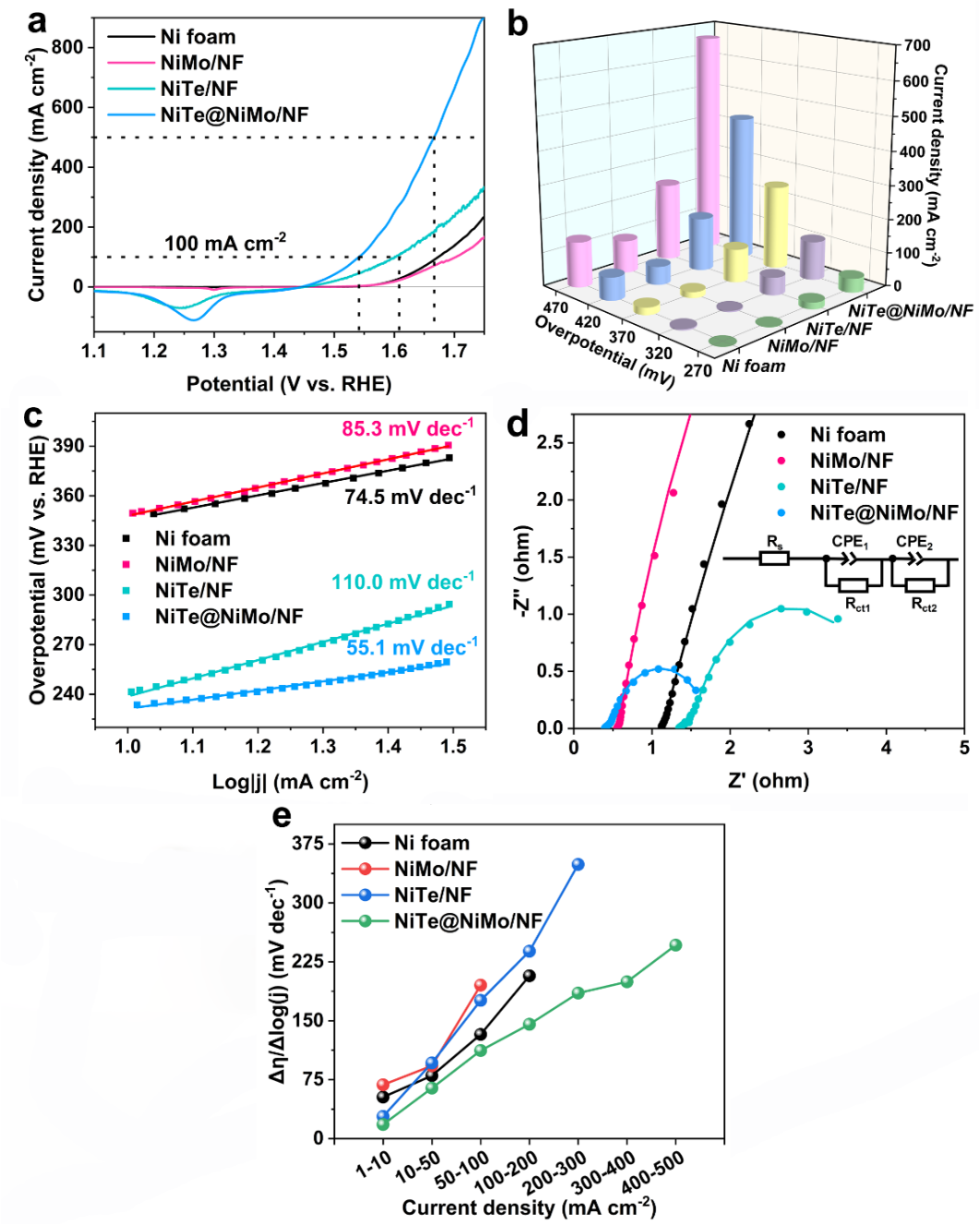

Fig. S9. The OER performance of NiTe@NiMo/NF and other control electrodes toward simulated seawater electrolysis. (a) Polarization curves acquired in simulated alkaline seawater (1.0 M KOH + 0.5 M NaCl). Scan rate: 2 mV s^{-1}. (b) Comparison of current densities achieved by different electrodes at various overpotentials. (c) Tafel plots. (d) Nyquist plots. (e) The $R_{\eta/j}$ plot of the electrodes in different current density ranges.

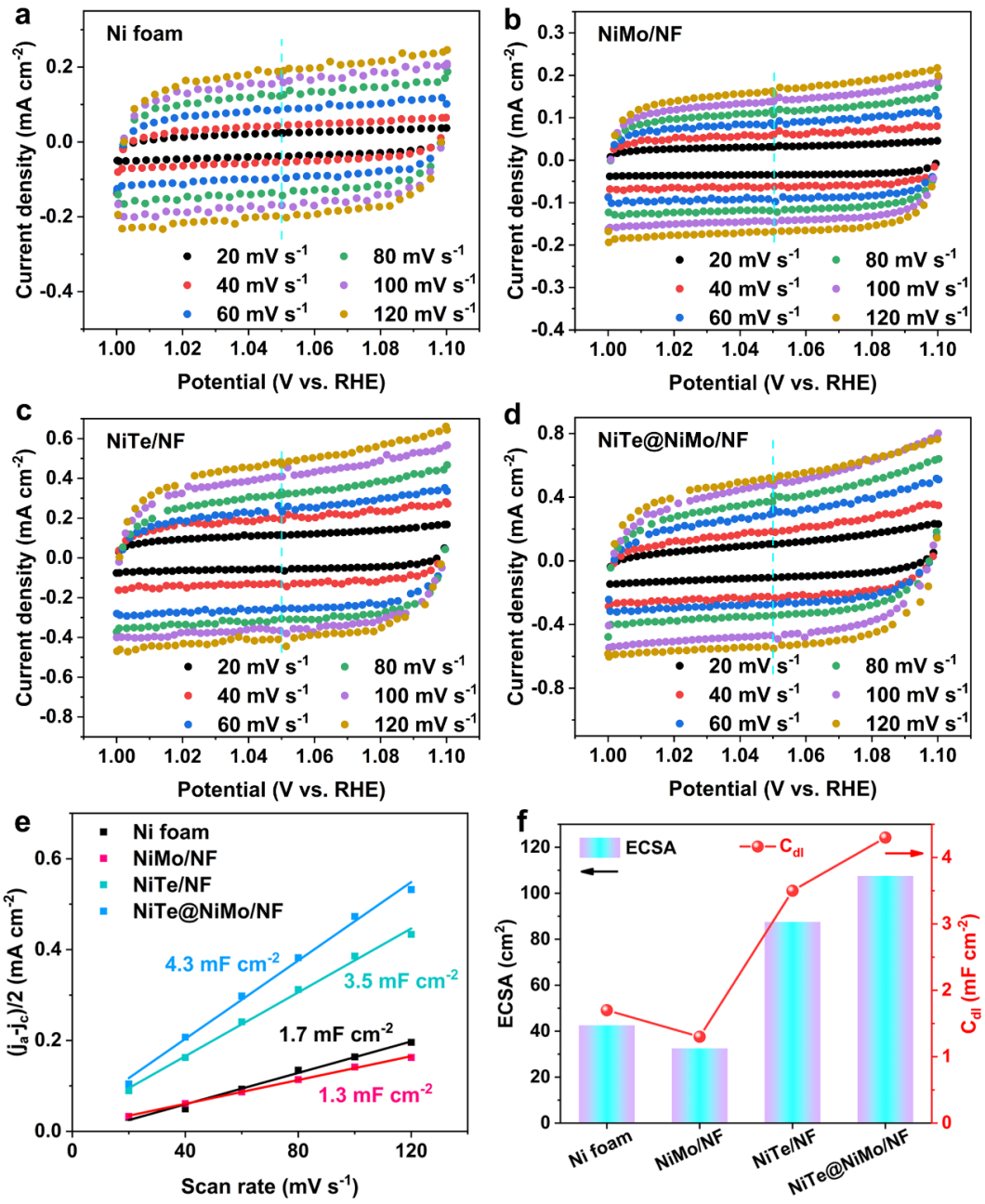

Fig. S10. CV curves acquired at different scan rates in the non-Faradaic range in simulated alkaline seawater (1.0 M KOH + 0.5 M NaCl) for (a) bare Ni foam, (b)NiMo/NF, (c) NiTe/NF and (d) NiTe@NiMo/NF electrodes. (e) C_{dl} plots and (f) ECSA values of NiTe@NiMo/NF and other controls.

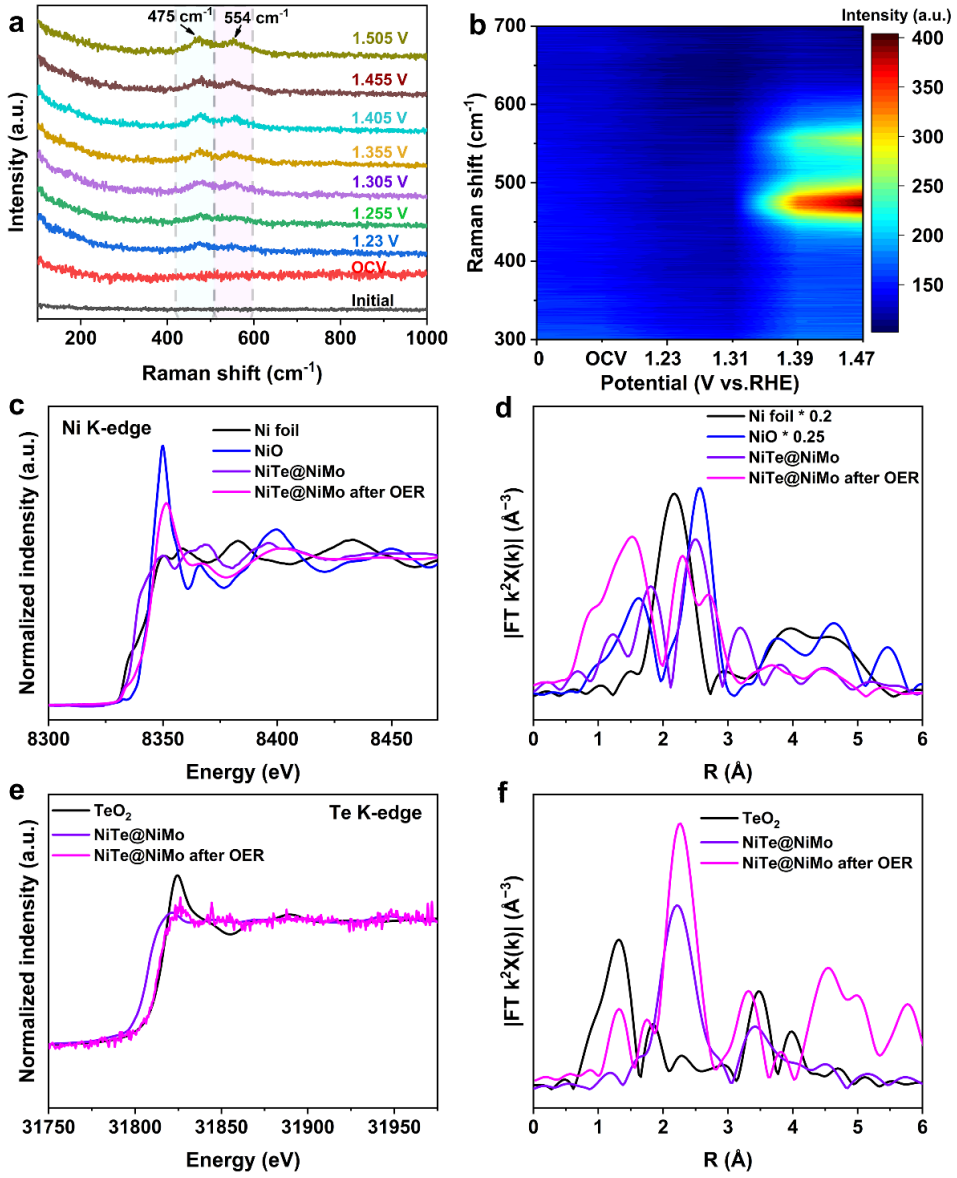

Fig. S11. In-situ Raman spectra of the (a) NiTe/NF and (b) NiTe@NiMo/NF electrodes. (c) Ni K-edge XANES spectra. (d) Fourier transforms of the k^2-weighted Ni K-edge EXAFS spectra. (e) Te K-edge XANES spectra. (f) Fourier transforms of the k^2-weighted Te K-edge EXAFS spectra of NiTe@NiMo during the OER in simulated alkaline seawater (1.0 M KOH + 0.5 M NaCl). Note: Given the bulk sensitivity of the XAS in the energy range under study, the signal appearing at ~2.4 Å in panel (d) likely results from the interference of the interior NiTe and some incidentally introduced metallic Ni impurities when NiTe@NiMo was scraped from the Ni foam current collector, along with amorphization of Ni species.

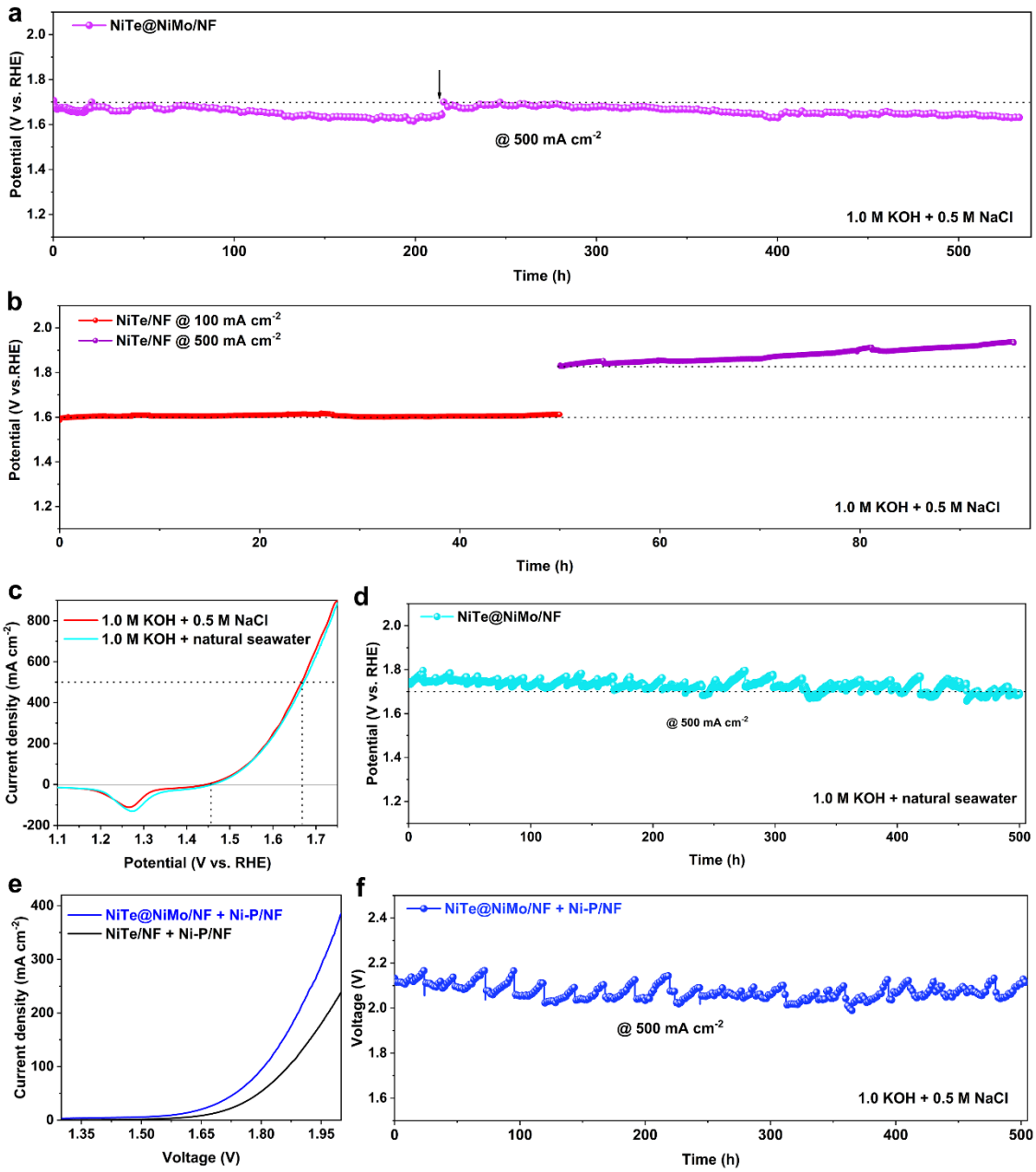

Fig. S12. (a) Long-term stability of the NiTe@NiMo/NF electrode evaluated in simulated alkaline seawater at 500 mA cm^{-2}. (b) Long-term catalytic stability of the NiTe/NF electrode at 100 and 500 mA cm^{-2}. (c) Polarization curves of the NiTe@NiMo/NF electrode recorded in alkaline simulated and natural seawater. Scan rate: 2 mV s^{-1}. (d) Long-term OER stability of the NiTe@NiMo/NF electrode assessed in alkaline natural seawater at 500 mA cm^{-2}. (e) Polarization curves of the NiTe@NiMo/NF || Ni-P/NF and NiTe/NF || Ni-P/NF electrode pairs for overall simulated seawater electrolysis in 1.0 M KOH + 0.5 M NaCl. (f) Long-term stability

of the NiTe@NiMo/NF || Ni-P/NF electrode pair for overall simulated seawater electrolysis at 500 mA cm^{-2}. The fluctuations in panels (d) and (f) result from the electrolyte consumption and replenishment.

The outstanding OER stability of the NiTe@NiMo/NF electrode at 500 mA cm^{-2} can be explained as follows: firstly, the potential at 500 mA cm^{-2} is lower than the CER onset potential so that there is virtually no corrosive hypochlorite species produced; secondly, the electrodeposited amorphous NiMo serves as a passivation layer protecting the underlying NiTe and metallic Ni substrate from dissolution; last but not least, the presence of $[MoO_4]^{2-}$ groups on the electrode surface helps to repel Cl^- ions, mitigating their possible corrosion.

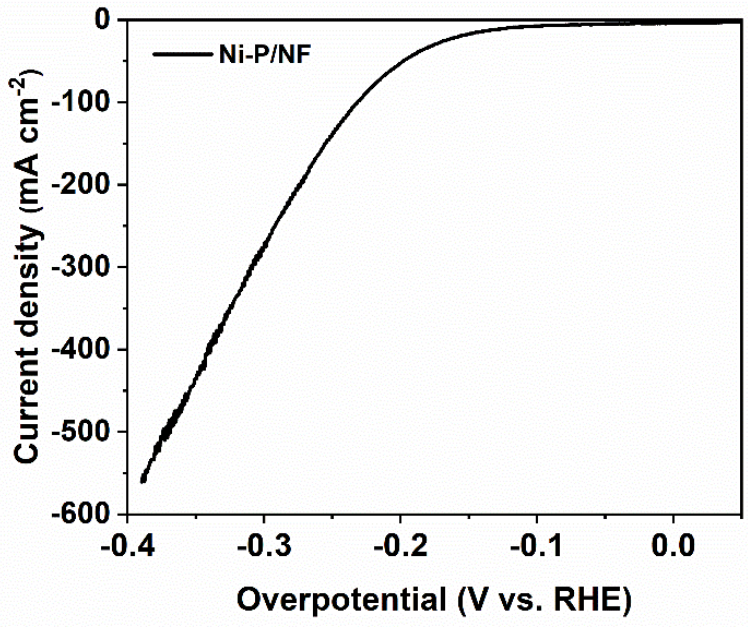

Fig. S13. The HER polarization curve of the Ni-P/NF electrode acquired in simulated alkaline seawater solution (1.0 M KOH + 0.5 M NaCl). Scan rate: 2 mV s^{-1}.

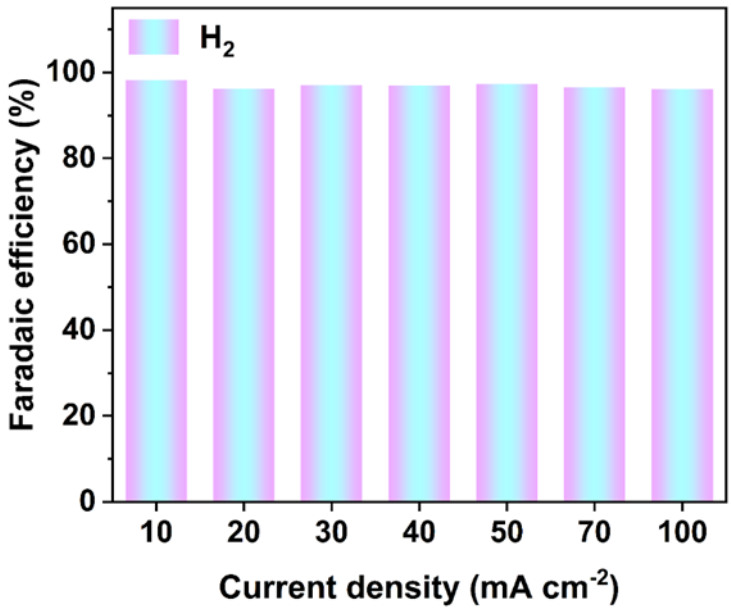

Fig. S14. Faradaic efficiency of H_2 production in the cathodic compartment of the NiTe@NiMo/NF || Ni-P/NF system.

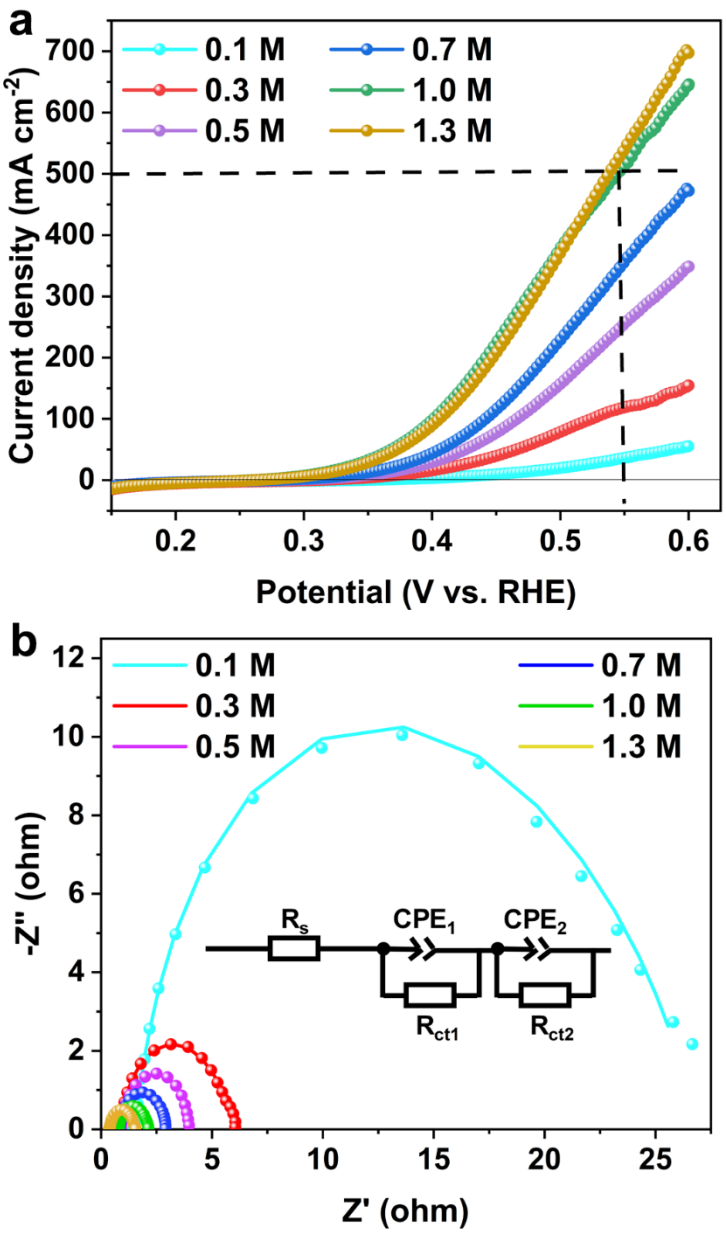

Fig. S15. SOR assisted asymmetric seawater electrolysis performance measured in simulated seawater (1.0 M KOH + 0.5 M NaCl). (a) Polarization curves for the NiTe@NiMo/NF electrode recorded in simulated seawater containing different concentrations of $Na_2S{\cdot}9H_2O$. (b) Nyquist plots. Inset: the equivalent circuit model used for fitting.

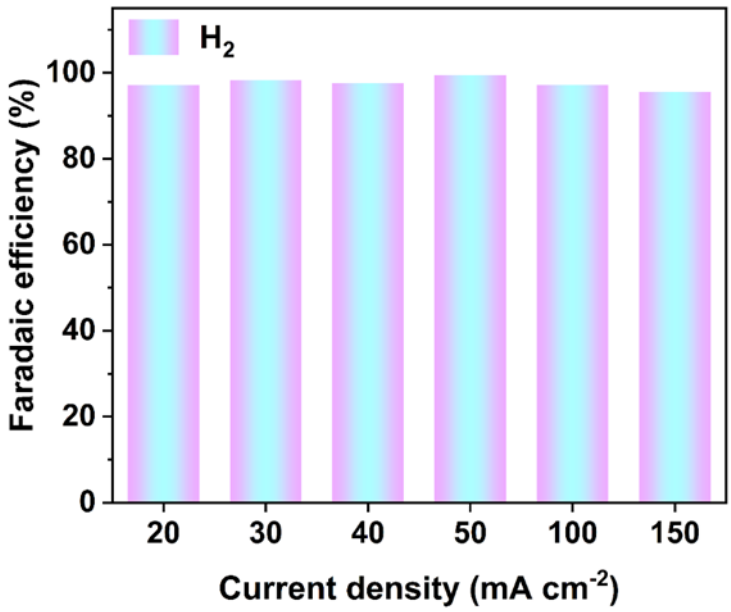

Fig. S16. Faradaic efficiency of H_2 production at the cathode at various current densities, when coupled with the anodic SOR.

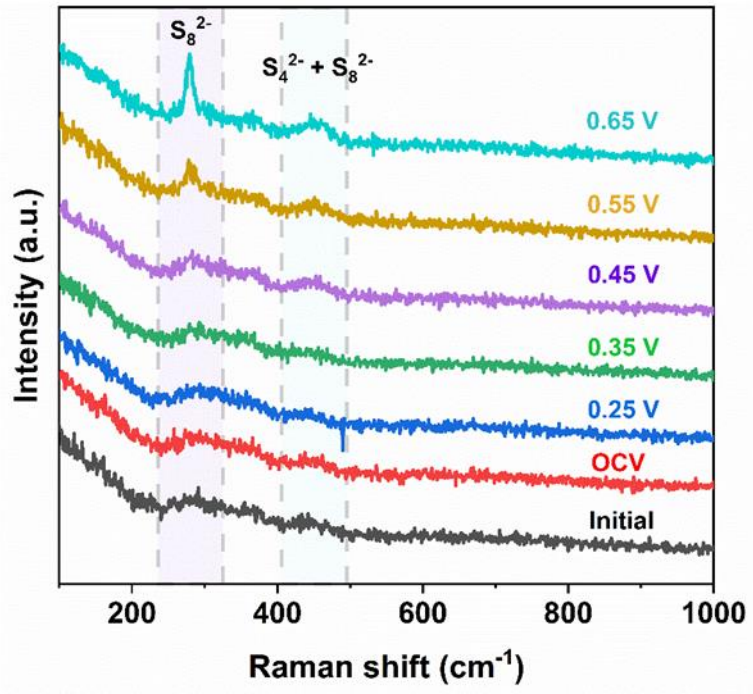

Fig. S17. In-situ Raman spectra of the NiTe@NiMo/NF electrode during the SOR in 1.0 M KOH + 0.5 M NaCl + 1.0 M $Na_2S \cdot 9H_2O$.

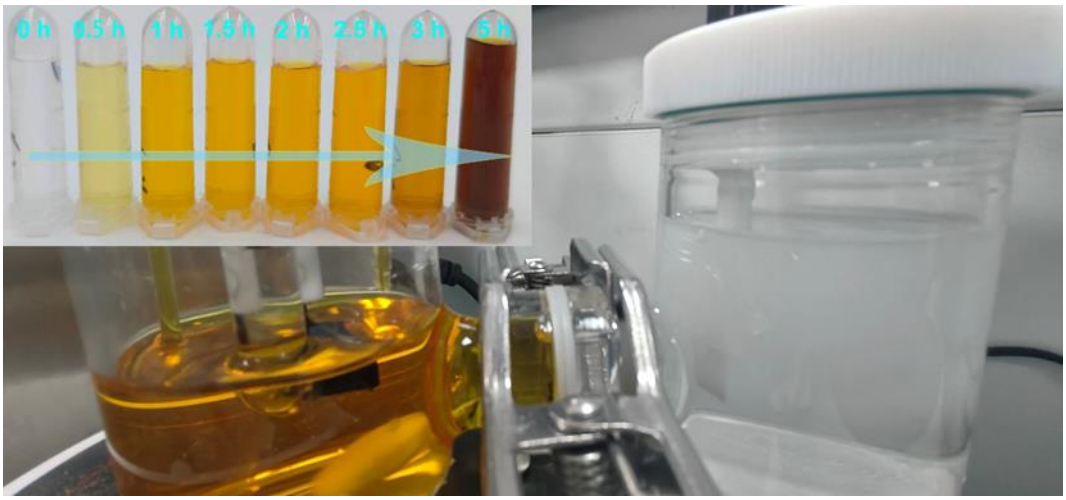

Fig. S18. Digital photograph showing the asymmetric SOR assisted simulated seawater electrolysis cell. Inset: digital photographs showing the evolution of the appearance of the anolyte over time.

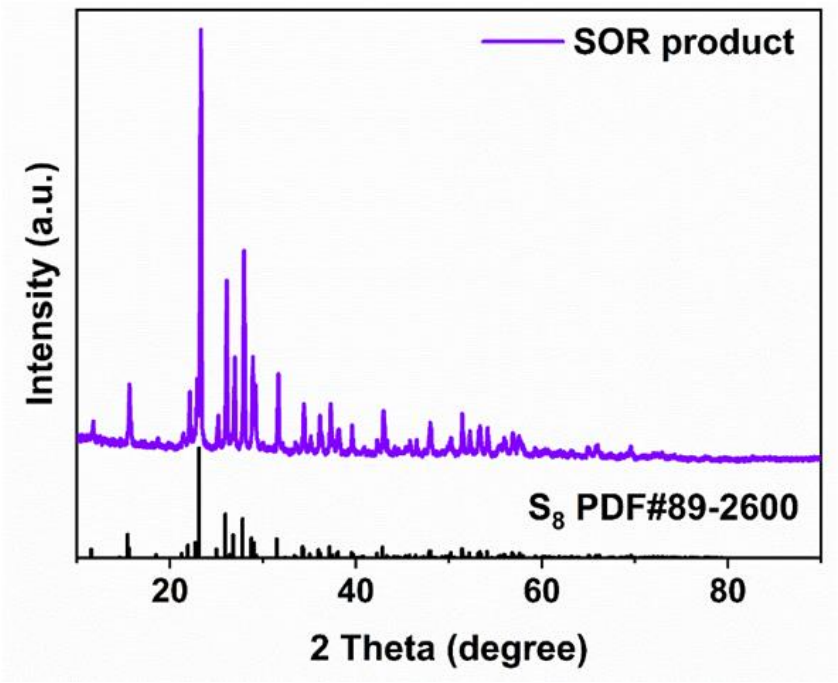

Fig. S19. XRD pattern of the solid product collected upon acidification of the anolyte after the SOR. The standard diffraction pattern of elemental sulfur is given for comparison.

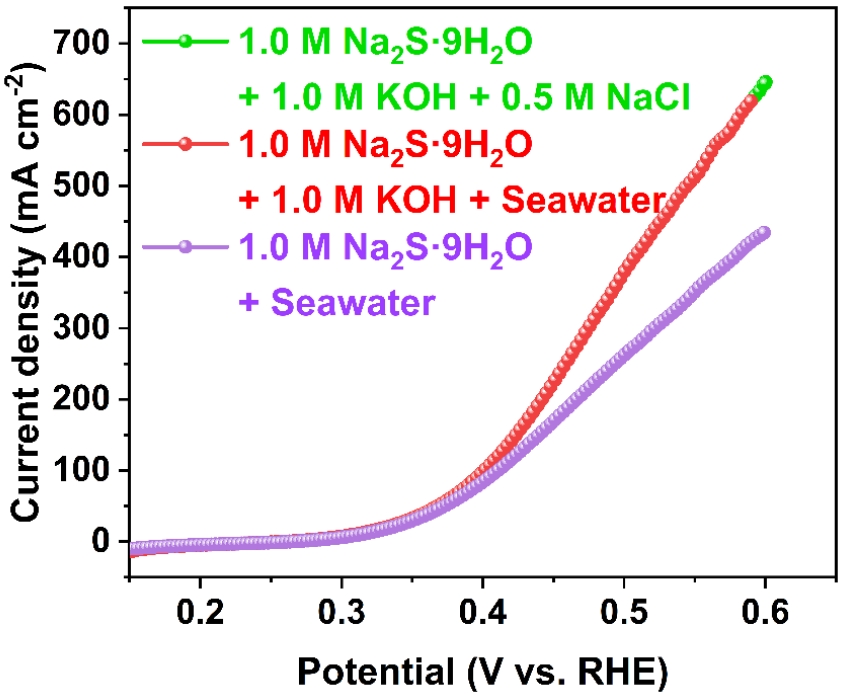

Fig. S20. Comparison of SOR polarization curves of the NiTe@NiMo/NF electrode in simulated and natural seawater solutions containing 1.0 M $Na_2S·9H_2O$.

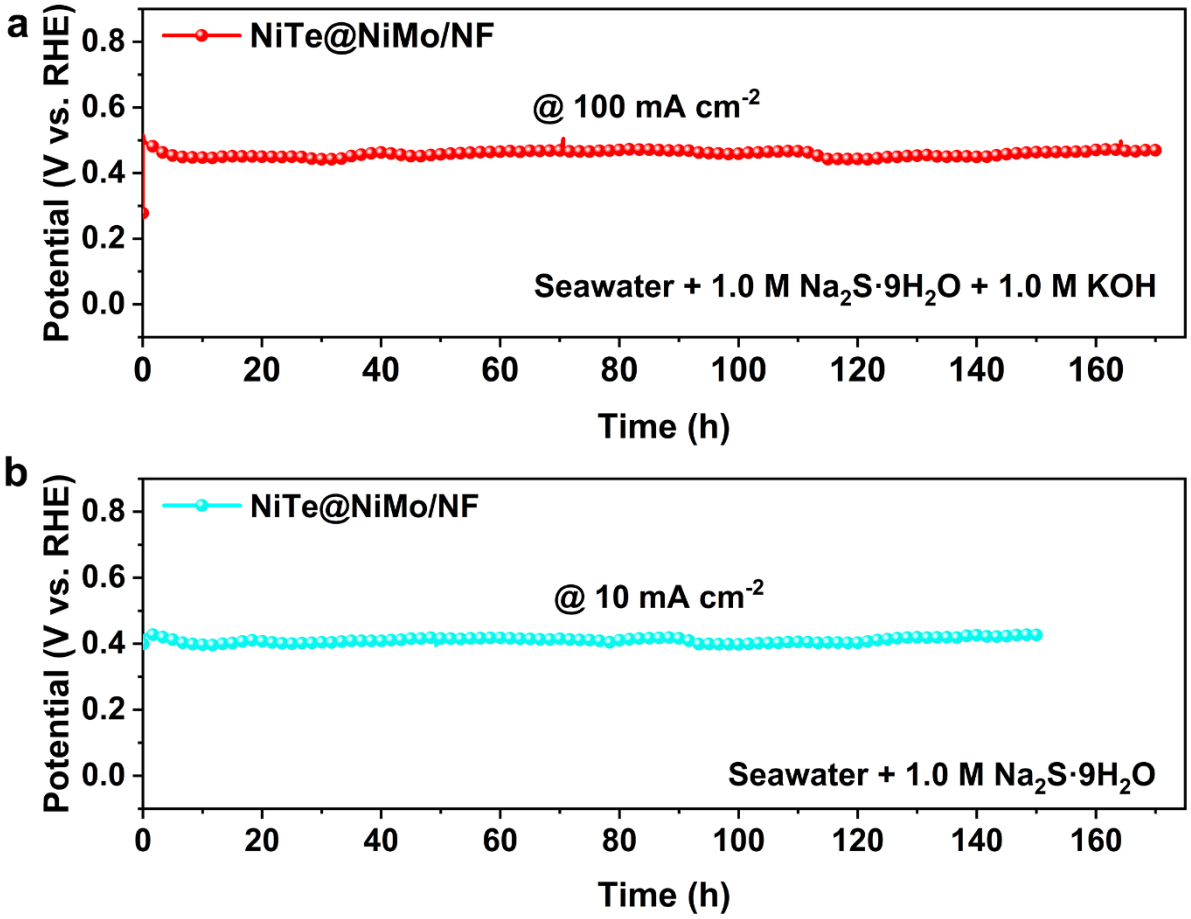

Fig. S21. Long-term SOR stability of the NiTe@NiMo/NF electrode recorded in alkaline natural seawater. (a) seawater + 1.0 M $Na_2S·9H_2O$ + 1.0 M KOH. (b) seawater + 1.0 M $Na_2S·9H_2O$.

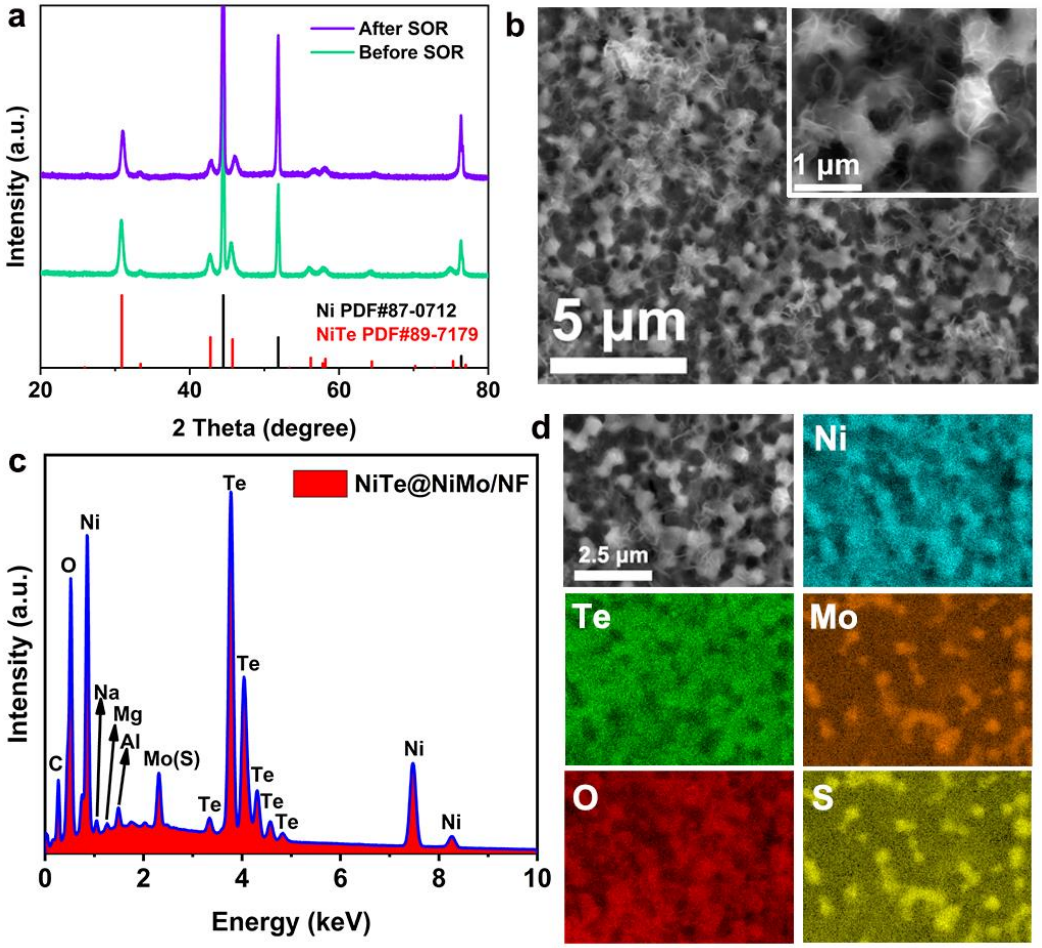

Fig. S22. (a) XRD patterns, (b) SEM, (c) SEM-EDS spectrum and (d) elemental mapping of the NiTe@NiMo/NF electrode after the SOR at 1.0 A cm^{-2} in natural seawater for 334 h in the flow cell.

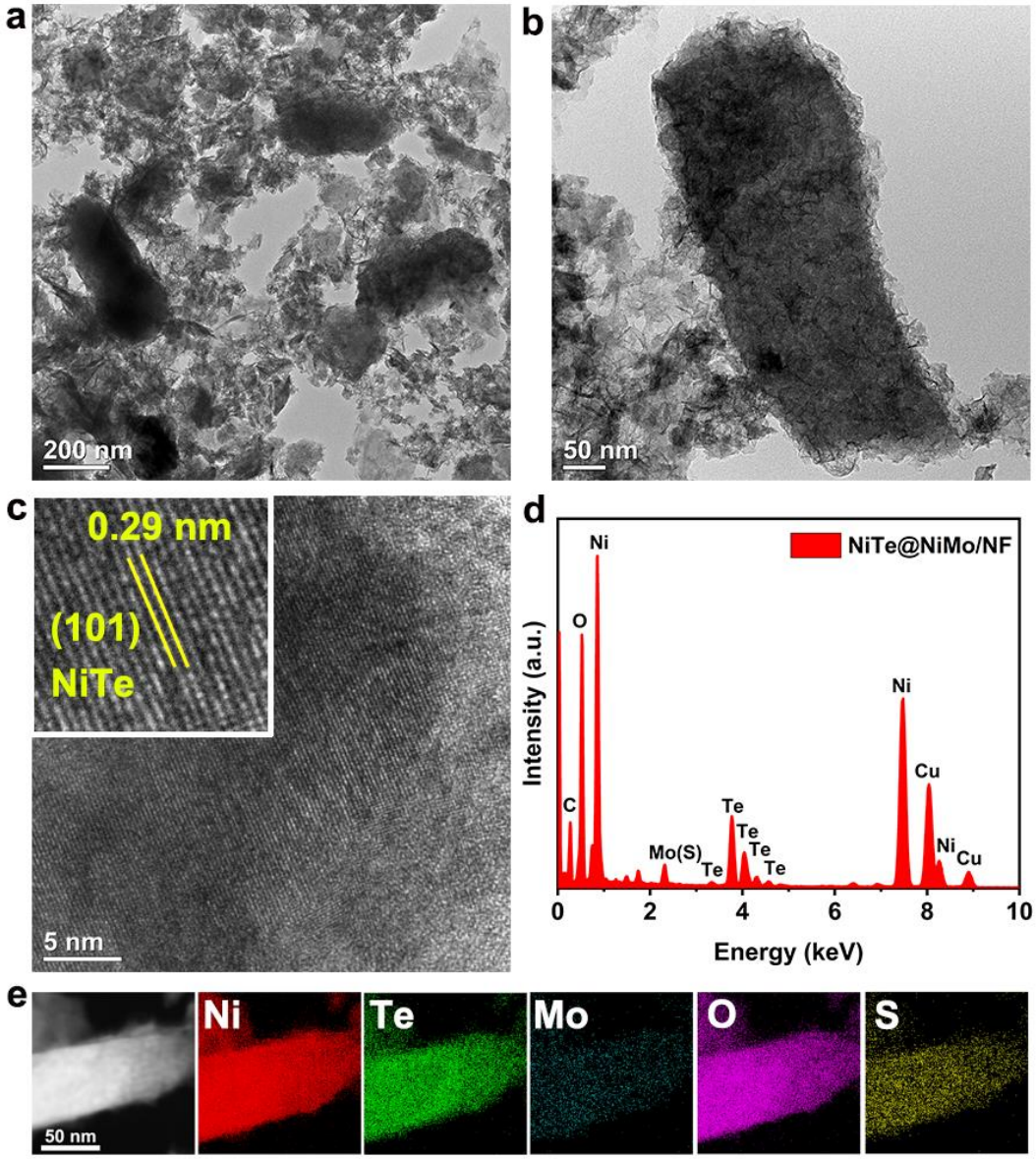

Fig. S23. (a-b) TEM, (c) HRTEM (Inset: zoomed view), (d) TEM-EDS spectrum and (e) elemental mapping of the NiTe@NiMo/NF electrode after the SOR at 1.0 A cm^{-2} in natural seawater for 334 h.

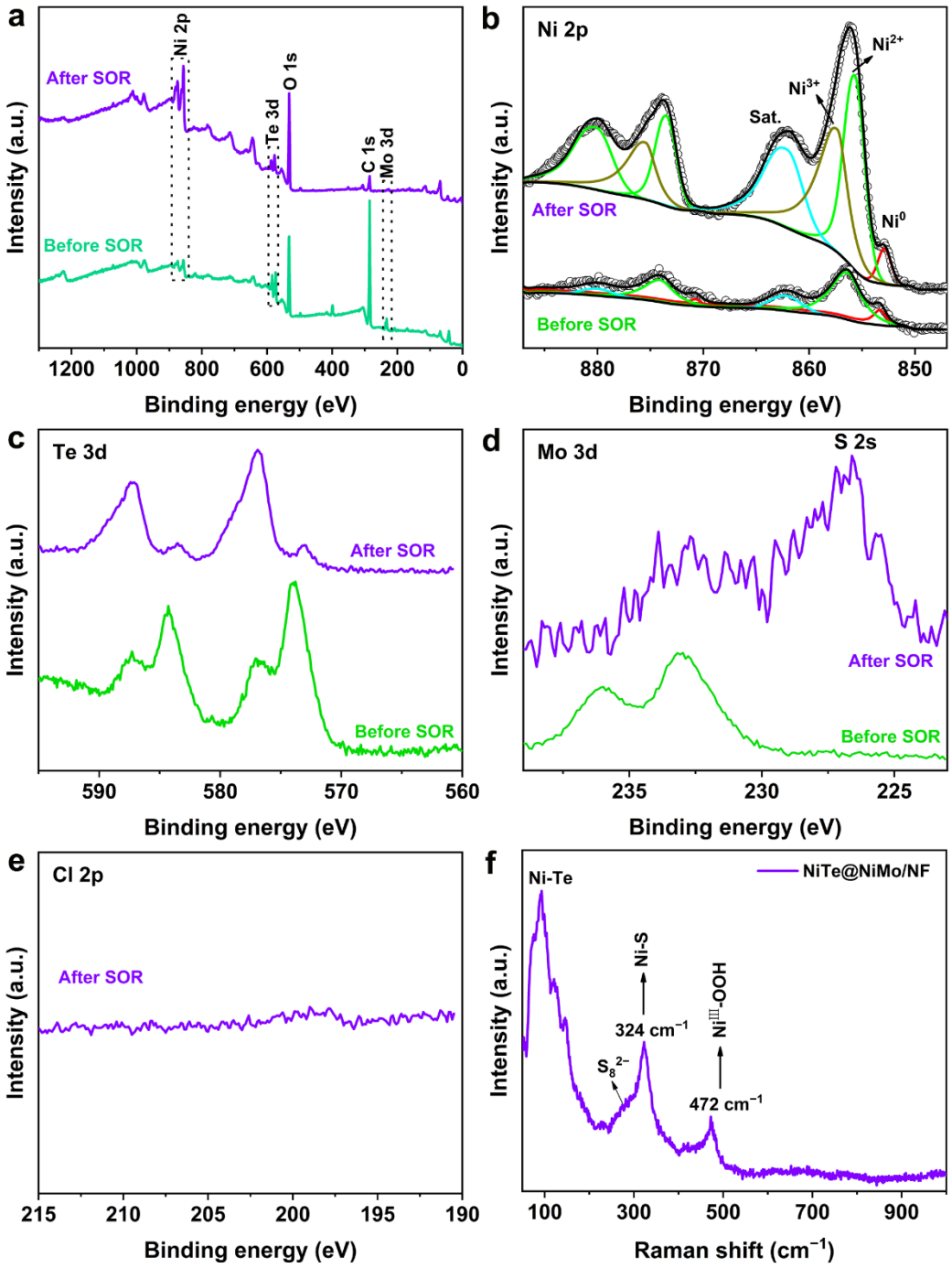

Fig. S24. The XPS characterization of the NiTe@NiMo/NF electrode before and after the SOR at 1.0 A cm^{-2} in alkaline natural seawater for 334 h. (a) XPS survey spectra. High-resolution XPS spectra of (b) Ni 2p, (c) Te 3d, (d) Mo 3d and (e) Cl 2p. (f) Raman spectrum of the NiTe@NiMo/NF electrode after the SOR. The post-SOR electrode was carefully rinsed by DI water before measurements to avoid the interference of surface-adsorbed polysulfides to XPS and Raman signals.

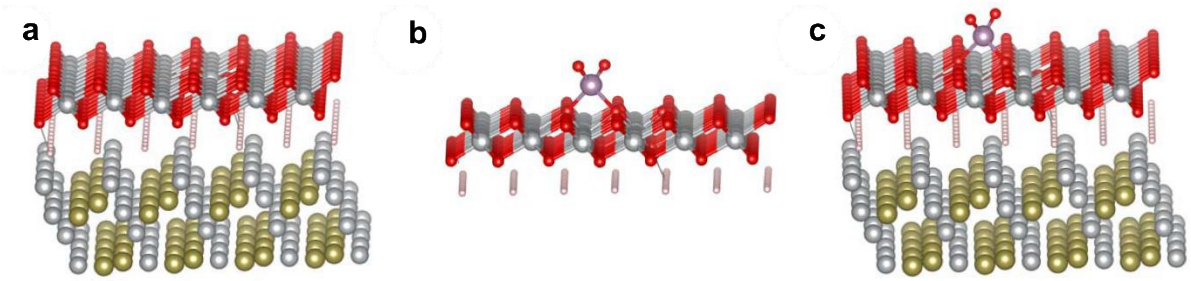

Fig. S25. Structure configurations of (a) NiTe/NiOOH, (b) NiOOH@MoO_4^{2-} and (c) NiTe/NiOOH@MoO_4^{2-}. Gray, dark yellow, red, pink and purple spheres represent Ni, Te, O, H and Mo atoms, respectively.

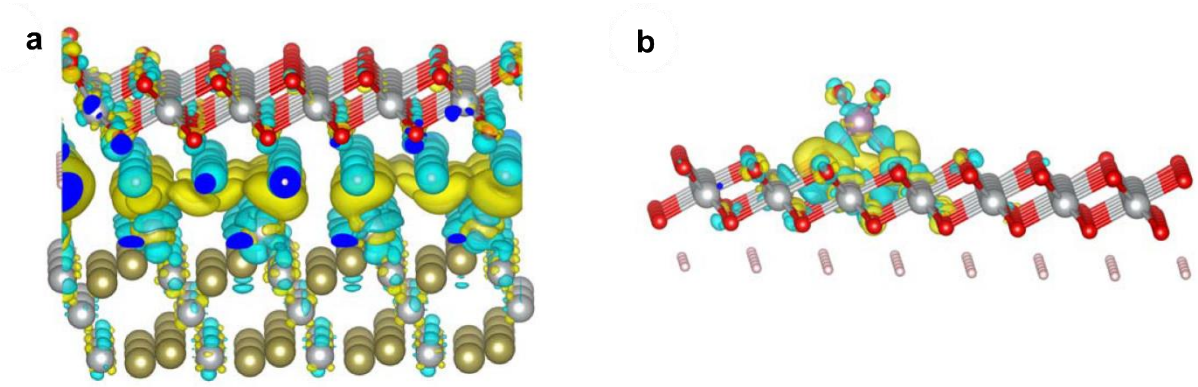

Fig. S26. Charge density difference images of the (a) NiTe/NiOOH and (b) MoO_4^{2-} absorbed NiOOH. Yellow and blue regions represent electron accumulation and depletion, respectively. Gray, dark yellow, red, pink and purple spheres represent Ni, Te, O, H and Mo atoms, respectively.

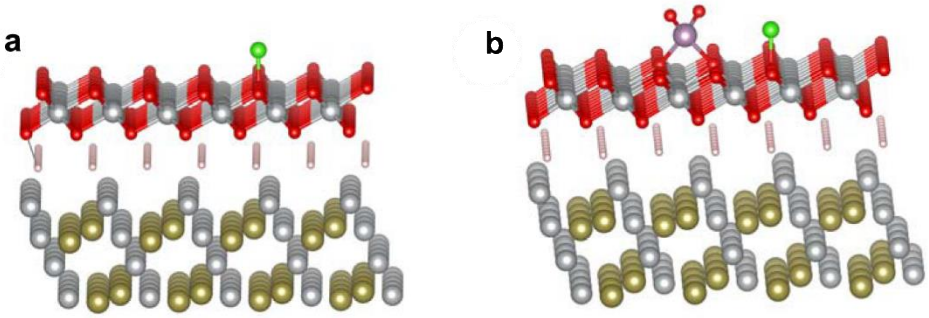

Fig. S27. The adsorption configuration of chloride ions on (a) NiTe/NiOOH; (b) NiTe/NiOOH@MoO_4^{2-}. Gray, dark yellow, red, pink, purple and green spheres represent Ni, Te, O, H, Mo and Cl atoms, respectively.

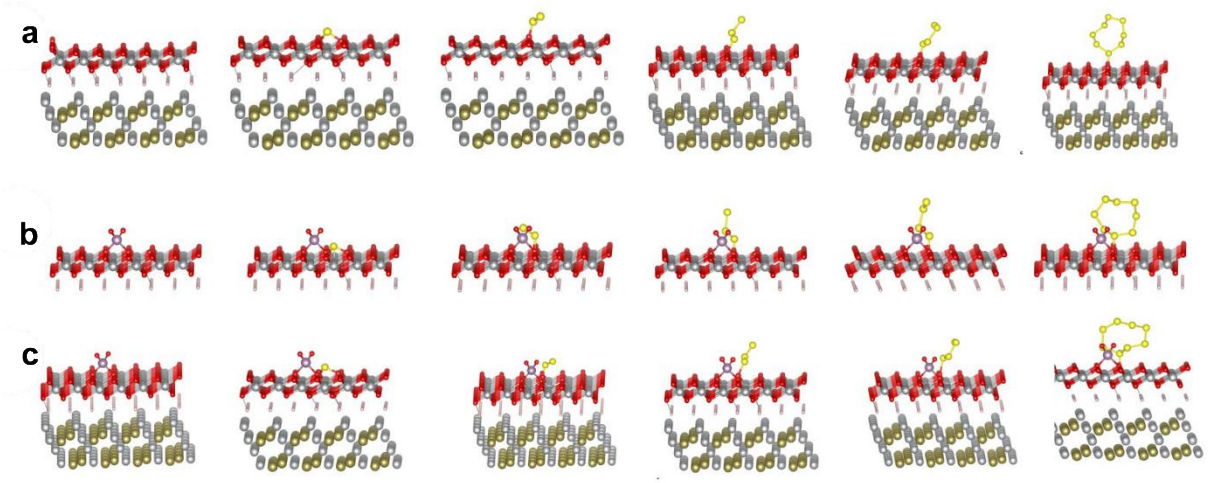

Fig. S28. The adsorption structure of *S, *S_2, *S_3, *S_4 and *S_8 intermediates on (a) NiTe/NiOOH, (b) NiOOH@MoO_4^{2-} and (c) NiTe/NiOOH@MoO_4^{2-}. Gray, dark yellow, red, pink, purple and yellow spheres represent Ni, Te, O, H, Mo and S atoms, respectively.

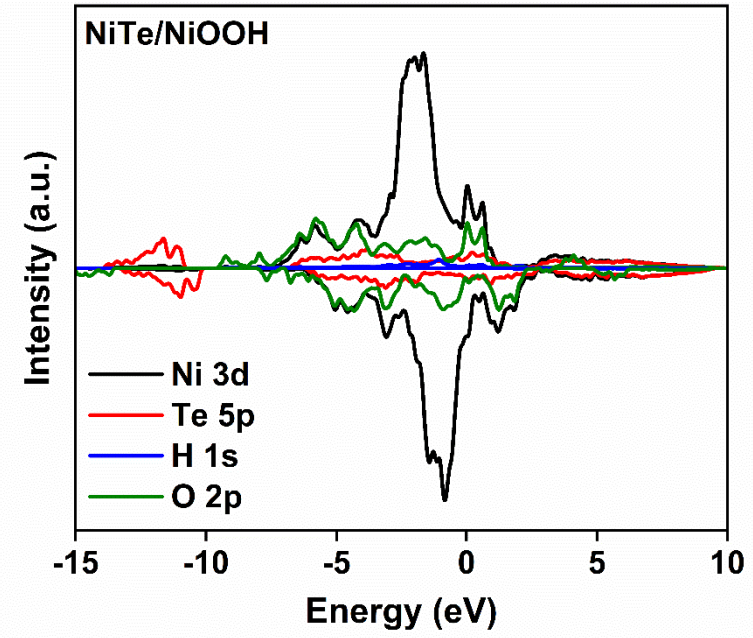

Fig. S29. Projected density of state (PDOS) for NiTe/NiOOH.

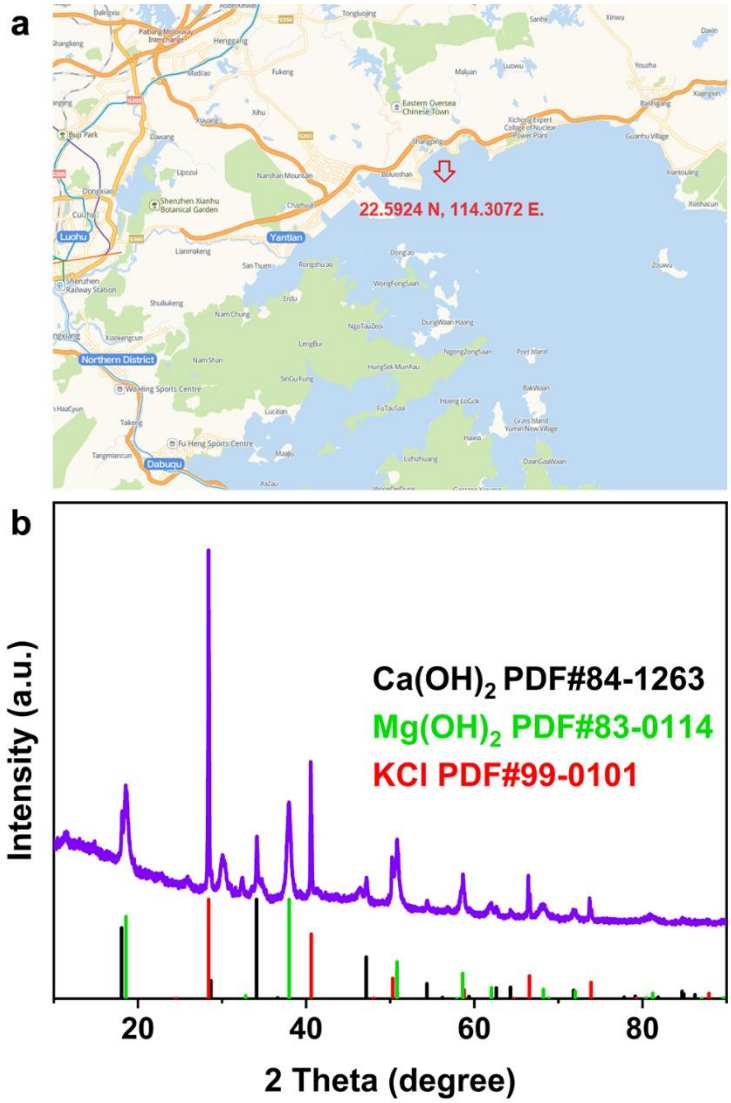

Fig. S30. (a) Location (Dapengwan, Shenzhen, China) and time (October 14, 2023) of natural seawater acquisition. (b) XRD patterns of the solid product obtained by alkali treatment of natural seawater. 1.0 M KOH was used for the alkalization. For reference, the standard diffraction patterns of $Ca(OH)_2$, $Mg(OH)_2$ and KCl are also presented.

Table S1. The fitting parameters of the Potentiostatic Electrochemical Impedance Spectroscopy (PEIS) data for different electrodes toward the OER in simulated alkaline-saline water (**Fig.s S2** and **S10**).

Catalyst	R_s (Ω)	R_{ct1} (Ω)	R_{ct2} (Ω)	Electrolyte	Potential (V vs. RHE)
Ni foam	1.13	53.99	/	1.0 KOH + 0.5 M NaCl	1.50
NiMo/NF	0.55	0.02	30.4		
NiTe/NF	1.33	0.50	2.23		
NiTe@NiMo/NF-1 min	0.55	0.47	1.92		
NiTe@NiMo/NF-3 min	0.53	0.22	1.70		
NiTe@NiMo/NF-5 min	0.39	0.15	1.18		
NiTe@NiMo/NF-8 min	0.39	0.14	1.28		
NiTe@NiMo/NF-10 min	0.64	0.17	1.49		

Table S2. Structural parameters derived from nonlinear least-squares fits to the first peak of the Fourier transform EXAFS spectra at the Te K-edge and Mo K-edge for the NiTe and NiTe@NiMo catalysts.

Catalyst	Path	r (Å)	σ^2 (Å^2)	ΔE_0 (eV)	N	R factor
NiTe	Te–Ni	2.629 ± 0.008	0.008 ± 0.001	7.850 ± 1.324	6.0	0.007
NiTe@NiMo	Te–Ni	2.629 ± 0.008	0.008 ± 0.001	8.571 ± 1.277	5.964 ± 0.711	0.007
NiTe@NiMo	Mo–O	1.777 ± 0.011	0.002 ± 0.001	−5.004 ± 2.917	3.970 ± 0.641	0.014

r: bond distance;

σ^2: Debye-Waer factors;

ΔE_0: the inner potential correction;

N: coordination number;

R factor: goodness of fit.

S_0^2 was set to 0.81 for Te and 0.85 for Mo.

For Te EXAFS fitting, the data ranges are presented as follows: $2.95 \leq k \leq 11.9$ Å^{-1}, $1.4 \leq R \leq 2.7$ Å. The independent point is 7.30 and the number of variables is 4.

For Mo EXAFS fitting, the data ranges are presented as follows: $3.5 \leq k \leq 12.9$ Å^{-1}, $1.0 \leq R \leq 2.1$ Å. The independent point is 6.39 and the number of variables is 4.

Table S3. The fitting parameters of the PEIS data for the NiTe@NiMo/NF electrode toward the SOR in 1.0 KOH + 0.5 M NaCl + x M $Na_2S·9H_2O$ electrolyte (**Fig. S15**).

Catalyst	R_s (Ω)	R_{ct1} (Ω)	R_{ct2} (Ω)	Concentration of $Na_2S·9H_2O$ (x)	Potential (V vs. RHE)
NiTe@NiMo/NF	1.48	11.13	14.25	0.1 M $Na_2S·9H_2O$	0.4
	0.81	3.02	2.35	0.3 M $Na_2S·9H_2O$	
	0.84	3.02	0.12	0.5 M $Na_2S·9H_2O$	
	0.78	2.10	0.06	0.7 M $Na_2S·9H_2O$	
	0.77	1.33	0.03	1.0 M $Na_2S·9H_2O$	
	0.35	0.95	0.35	1.3 M $Na_2S·9H_2O$	

Table S4. Performance comparison of various SOR-assisted water(seawater) electrolysis systems reported so far in the literature.

Catalyst	electrolyte	Current density (mA cm^{-2})	Potential (V vs. RHE)	Stability	Ref.
NiTe@NiMo/NF	**1 M NaOH + 0.5 M NaCl + 1 M $Na_2S·9H_2O$**	**500**	**0.55**	**100 h @ 500 mA cm^{-2}**	**This work**
CoNi@NGs	1 M NaOH + 1 M Na_2S	90	0.5	500 h @ 0.317 V vs. RHE	S8
$CoFeS_2$(3:1)	0.77 M H_2S + 1 M NaOH	200	0.6	120 h @ 0.3 V vs. RHE	S9
NiCu–MoS_2	0.75 M H_2S + 1 M NaOH	303	0.65	150 h @ 0.3 V vs. RHE	S10
Co-Ni_3S_2	1 M NaOH + 1 M Na_2S	100	0.59	24 h @ 50 mA cm^{-2}	S11
Fe_3C@N-CNTs/IF	1 M NaOH + 1 M Na_2S	10	0.46	36 h @ 0.7 V vs. RHE	S12
CoS_2@C/MXene/NF	1 M NaOH + 1 M Na_2S	300	0.648	240 h @ 0.723 V vs. RHE	S13
Co-S NSs	1 M NaOH + 0.5 M Na_2S	100	0.44	72 h @ 0.5 V vs. RHE	S14
S-Cu:Co@NF	1 M KOH+1 M K_2S	175.3	0.5	16 h @ 100 mA cm^{-2}	S15

Table S5. The fitting parameters of the PEIS data for the control samples toward the SOR (**Fig. 3**).

Catalyst	R_s (Ω)	R_{ct1} (Ω)	R_{ct2} (Ω)	Electrolyte	Potential (V vs. RHE)
Ni foam	0.97	4.80	16.52	1.0 M KOH + 0.5 M NaCl + 1.0 M $Na_2S·9H_2O$	0.4
NiMo@NF	0.81	0.32	3.39		
NiTe/NF	0.77	0.72	0.57		
RuO_2	0.48	10.28	13.4		
Pt/C	0.44	2.82	0.29		

Table S6. Room-temperature conductivity and pH values of different electrolytes used in this work.

Electrolyte	Conductivity (mS cm^{-1})	pH
1.0 M KOH + 0.5 M NaCl	243.9	13.7
1.0 M KOH + seawater	225.2	13.9
1.0 M KOH + 0.5 M NaCl + 1.0 M $Na_2S·9H_2O$	317.5	13.7
1.0 M KOH + seawater + 1.0 M $Na_2S·9H_2O$	304.6	13.7
seawater + 1.0 M $Na_2S·9H_2O$	182.5	13.4
as-collected seawater	46.9	7.9

Table S7. Electrocatalytic performance comparison of the hybrid natural seawater electrolysis systems reported recently in the literature.

Anode reaction	Anode catalyst	Anolyte	Cathode catalyst	Cell voltage [V] (current density [mA cm^{-2}])	Ref.
SOR	**NiTe@NiMo/ NF**	**1 M KOH + seawater + 2 M $Na_2S·9H_2O$**	**Ni-P/NF**	**0.7 (1000) @ 70 °C**	**This work**
EGOR (ethylene glycol oxidation reaction)	Rh/RhOOH metallene	1 M KOH + seawater + 6 M $(CH_2OH)_2$	Rh/RhOOH metallene	0.678 (10)	S16
XOR (xylose oxidation reaction)	NiCoP	1 M KOH + seawater + 100 mM $C_5H_{10}O_5$	NiCoP	1.57 (100)	S17
MOR (methanol oxidation reaction)	$NiFe_2O_4$/NF	1 M KOH + seawater + 0.5 M CH_3OH	$NiFe_2O_4$/NF	1.74 (100)	S18
	Pt-Co_3O_4/CP	seawater + 2.0 M CH_3OH	Pt-Co_3O_4/CP	1.5 (183.7)	S19
UOR (urea oxidation reaction)	Ru/P-$NiMoO_4$@NF	1 M KOH + seawater + 0.5 M $CO(NH_2)_2$	Ru/P-$NiMoO_4$@NF	1.73 (500)	S20
	Se/$NiSe_2$/NF	1 M KOH + seawater + 0.33 M $CO(NH_2)_2$	Se/$NiSe_2$/NF	1.71 (100)	S21
HzOR (hydrazine oxidation reaction)	Mo-Ni_2P_v@MNF	1 M KOH + seawater + 0.5 M N_2H_4	Mo-Ni_2P_v@MNF	0.571 (1000)	S22
	MIL-(IrNiFe)@NF	1.0 M KOH + seawater + 0.5 M N_2H_4	MIL-(IrNiFe)@NF	0.39 (500)	S23

Table S8. The PDOS of active Ni, Mo, Te and O atom site in NiTe/NiOOH, NiOOH@MoO_4^{2-} and NiTe/NiOOH@MoO_4^{2-} (**Fig. 5d** and **5e**).

	NiTe/NiOOH		NiOOH@MoO_4^{2-}		NiTe/NiOOH@MoO_4^{2-}	
	Up	Down	Up	Down	Up	Down
Ni 3d band	−2.07	−1.21	−2.44	−2.28	−2.13	−1.26
Mo 4d band	/	/	−0.99	−0.93	−1.75	−0.87
Te 5p band	−1.52	−0.69	/	/	−1.71	−0.83
O 2P band	−3.48	−2.08	−2.62	−2.41	−3.37	−1.97
Δ(Ni-O)	1.41	0.87	0.18	0.13	1.24	0.71

References:

S1 H. Tan, Z. Yu, A. P. LaGrow, S. Ma, J. Wang, H. Li, D. Xiong and L. Liu, *J. Mater. Chem. A*, 2023, 11, 26152-26163.

S2 P. Guo, S. Cao, Y. Wang, X. Lu, Y. Zhang, X. Xin, X. Chi, X. Yu, I. Tojiboyev, H. Salari, A. J. Sobrido, M. Titirici and X. Li, *Appl. Catal., B*, 2022, 310, 121355.

S3 G. Kresse and J. Furthmüller, *Comput. Mater. Sci*, 1996, 6, 15-50.

S4 G. Kresse and J. Hafner, *Phys. Rev. B*, 1993, 47, 558-561.

S5 G. Kresse and D. Joubert, *Phys. Rev. B*, 1999, 59, 1758-1775.

S6 R. Dronskowski and P. E. Bloechl, *J. Phys. Chem.*, 1993, 97, 8617-8624.

S7 S. Maintz, V. L. Deringer, A. L. Tchougréeff and R. Dronskowski, *J. Comput. Chem.*, 2016, 37, 1030-1035.

S8 M. Zhang, J. Guan, Y. Tu, S. Chen, Y. Wang, S. Wang, L. Yu, C. Ma, D. Deng and X. Bao, *Energy Environ. Sci.*, 2020, 13, 119-126.

S9 M. Kumar and T. C. Nagaiah, *J. Mater. Chem. A*, 2022, 10, 7048-7057.

S10 M. Kumar and T. C. Nagaiah, *J. Mater. Chem. A*, 2022, 10, 13031-13041.

S11 Y. Li, Y. Duan, K. Zhang and W. Yu, *Chem. Eng. J.*, 2022, 433, 134472.

S12 W. Yu, J. Yu, Y. Wang, X. Li, Y. Wang, H. Yuan, X. Zhang, H. Liu and W. Zhou, *Appl. Catal., B*, 2022, 310, 121291.

S13 L. Zhang, Z. Wang and J. Qiu, *Adv. Mater.*, 2022, 34, 2109321.

S14 X. Teng, K. Shi, L. Chen and J. Shi, *Angew. Chem. Int. Ed.*, 2024, 63, e202318585.

S15 K. Yang, N. Zhang, J. Yang, Z. Xu, J. Yan, D. Li and S. Liu, *Appl. Catal., B*, 2023, 332, 122718.

S16 Q. Mao, K. Deng, H. Yu, Y. Xu, Z. Wang, X. Li, L. Wang and H. Wang, *Adv. Funct. Mater.*, 2022, 32, 2201081.

S17 Y. Yang, R. Zou, J. Gan, Y. Wei, Z. Chen, X. Li, S. Admassie, Y. Liu and X. Peng, *Green Chem.*, 2023, 25, 4104-4112.

S18 X. Du, M. Tan, T. Wei, H. Kobayashi, J. Song, Z. Peng, H. Zhu, Z. Jin, R. Li and W. Liu, *Chem. Eng. J.*, 2023, 452, 139404.

S19 K. Xiang, Z. Song, D. Wu, X. Deng, X. Wang, W. You, Z. Peng, L. Wang, J.-L. Luo and X.-Z. Fu, *J. Mater. Chem. A*, 2021, 9, 6316-6324.

S20 L. Guo, J. Chi, J. Zhu, T. Cui, J. Lai and L. Wang, *Appl. Catal., B*, 2023, 320, 121977.

S21 S. Khatun and P. Roy, *J. Colloid Interface Sci.*, 2023, 630, 844-854.

S22 J. Chi, L. Guo, J. Mao, T. Cui, J. Zhu, Y. Xia, J. Lai and L. Wang, *Adv. Funct. Mater.*, 2023, 33, 2300625.

S23 X. Zhai, Q. Yu, G. Liu, J. Bi, Y. Zhang, J. Chi, J. Lai, B. Yang and L. Wang, *J. Mater. Chem. A*, 2021, 9, 27424-27433.